

Imaging of groundwater with nuclear magnetic resonance

Marian Hertrich

ETH Zurich, Swiss Federal Institute of Technology, Schafmattstrasse 33, 8093 Zurich, Switzerland

Received 18 October 2007; accepted 18 January 2008

Available online 19 February 2008

Keywords: Earth's field; Geophysics; Tomography; Hydrology; Surface loops

Contents

1. Introduction	227
2. Surface NMR measurements.	228
2.1. Basic principle	228
2.2. The surface NMR signal	229
2.2.1. The magnetic fields	230
2.2.2. The vector spin magnetization	231
2.2.3. The NMR signal for surface loops	231
2.2.4. Isolating the integral kernel	232
3. Inversion of surface NMR data	232
3.1. 1-D investigations: magnetic resonance sounding (MRS)	233
3.1.1. Fixed geometry inversion.	233
3.1.2. Variable geometry inversion.	234
3.1.3. Reliability of water content estimates	235
3.2. 2-D investigations: magnetic resonance tomography (MRT)	236
4. Relaxation	238
4.1. Relaxation processes in rocks	238
4.2. Acquisition of relaxation parameters.	239
4.3. Observed data.	239
4.4. Limitations of current schemes	240
5. Limitations of the surface NMR method	241
5.1. Influence of the Earth's magnetic field	241
5.2. Influence of the sub-surface conductivity distribution	241
6. Field data example.	243
7. Summary and conclusions	246
Acknowledgements	247
References	247

1. Introduction

The method of surface nuclear magnetic resonance (SNMR) is a relatively new geophysical technique that

exploits the NMR-phenomenon for a quantitative determination of the sub-surface distribution of hydrogen protons, i.e. water molecules of groundwater resources, by non-intrusive means. The idea to employ NMR techniques within the Earth's magnetic field to derive sub-surface water contents was first proposed by Varian [1]. It was

E-mail address: marian@aug.ig.erdw.ethz.ch

not until the late 1970s that a group of Russian scientists took up the idea and developed the first field-ready prototype of surface NMR equipment in the 1980s. It allowed for the first time the recording of NMR signals from groundwater at considerable depths in the Earth [2–4]. Numerous field applications with the Russian Hydro-scope-equipment encouraged the ongoing technical developments for about a decade [5–7]. They were supported by several studies on the modeling, inversion and processing of surface NMR data [8–10]. Surface NMR became better known to western scientists when the first commercial equipment was launched by Iris Instruments (France) in 1996. A few groups worldwide actively pursued the fundamental research and applications of surface NMR. Over the past decade the continuous progress and experience has been reported at periodic international workshops (Berlin 1999, Orleans 2003, Madrid 2006), and followed-up publishing special issues of peer reviewed journals devoted to surface NMR [11,12]. Continuous technical development of surface NMR measurements has been carried out and, recently, two new suites of surface NMR hardware have been made commercially available [13,14]. The new systems extend the available technical possibilities towards improved noise mitigation schemes and multi-channel recording.

Major advances in the development of surface NMR were triggered by a revision of the fundamental equations proposed by Weichman et al. [15,16]. The improved formulation allows the correct calculation of complex-valued signals of measurements on conductive ground [17] and the calculation of surface NMR signals with separated transmitter and receiver loops. The latter feature has been studied in detail by Hertrich and co-workers [18,19] which revealed that a series of measurements at multiple offsets along a profile provides sufficient sensitivity to allow for high resolution tomographic inversion. A fast and efficient tomographic inversion scheme has been developed that provides the correct imaging of 2-D sub-surface structures from a series of surface measurements [20].

Various geophysical techniques, like geoelectrics, electromagnetics, georadar and seismics, are routinely used in a structural mapping sense in hydrogeology, to delineate bedrock and sometimes determine depth of the water table and other major geological boundaries. But surface NMR is the only technique that allows a quantitative determination of the actual water content distribution in the sub-surface. Near surface aquifers are the major source of drinking water worldwide. Additionally, these aquifers might be substantially affected by cultural pollution, mismanagement and natural retreat in the ongoing climate change. But also in many other environmental problems groundwater plays a key role. Examples are unstable permafrost and hill-slope stability in the progressive global warming or dynamics of glaciers and ice-sheets. For those issues surface NMR may provide essential information in high resolution imaging of the sub-surface water content distribution and monitoring of groundwater dynamics.

In conventional NMR applications (e.g. spectroscopy, medical imaging, non-destructive material testing) the excitation of the spin magnetization is in most cases induced and recorded by uniform secondary magnetic fields such that the recorded signal amplitude can be calibrated by samples of known spin density and the experiment can be designed such that perfectly controlled flip angles are obtained. By contrast, in surface NMR none of these requirements can be met and the amplitude of the recorded signal has to be quantitatively derived for non-uniform fields and the resulting arbitrary flip angles. Therefore, in this review article, a comprehensive derivation of the surface NMR signal is given and the formulations of the problem for 1-D and 2-D conditions are presented. State-of-the-art inversion techniques are needed to derive sub-surface models of water content distribution from measured field data state-of-the-art inversion techniques are needed and are applied with appropriate estimates of the reliability of those models given. The observed NMR relaxation times may in general provide additional information about the aquifer properties by their dependency on the pore space geometry, but their determination and interpretation are somewhat limited compared to conventional laboratory NMR techniques. A short account is given on possible schemes of relaxation time determination and future directions of surface NMR research. Since measured surface NMR signals substantially depend on the local settings of the Earth's magnetic field and the sub-surface resistivity distribution, the dependency on these parameters is described and their variability throughout the Earth is shown and accounted for in terms of likely response. As an example of state-of-the-art surface NMR measurements, the inversion and interpretation of a real data set from a well-investigated test site is presented.

2. Surface NMR measurements

2.1. Basic principle

Exploration for groundwater using NMR techniques takes advantage of the spin magnetic moment of protons, i.e. the hydrogen atoms of water molecules. In a zero external magnetic field environment, the spin magnetic moment vectors are randomly oriented. In the presence of an applied static magnetic field, the vectors precess about the magnetic field and at thermal equilibrium between the water molecules, the distribution of spin magnetic moment vectors has an alignment that results in a small net magnetic moment along the field direction (i.e. a longitudinal magnetic moment; Fig. 1a). Within the Earth, the spin magnetic moment vectors precess around the Earth's magnetic field \mathbf{B}_0 at the Larmor frequency $\omega_L = -\gamma_p |\mathbf{B}_0|$, where the gyromagnetic ratio $\gamma_p = 0.26752 \times 10^{-9} \text{ s}^{-1} \text{ T}^{-1}$. Worldwide values for $|\mathbf{B}_0|$ vary between 25,000 nT around the equator and 65,000 nT at high latitudes, resulting in Larmor frequencies of 0.9–3.0 kHz, i.e. signals in the audio-frequency range. In surface NMR, an alternating

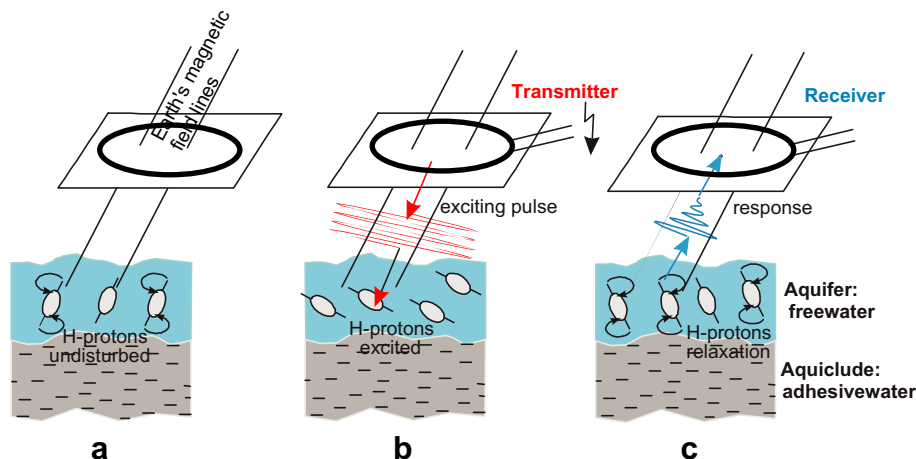


Fig. 1. Simplified sketches showing the principle of surface NMR in groundwater exploration. (a) A small percent of the protons are aligned with the Earth's magnetic field B_0 . (b) A small percent of the protons in an excited state. (c) Protons decaying (relaxing) back to their undisturbed state. The pulse moment “controls” the maximum penetration depth. The initial amplitude of the electromagnetic signal after the magnetic field has been turned off is heavily influenced by the water volume, and the shape of the decay curve provides information on the pore sizes. Modified from Ref. [50].

current $I(t)$ is passed through the transmitter loop for a period of $\tau_p \sim 40$ ms, generating a highly inhomogeneous magnetic field \mathbf{B}_1 throughout the sub-surface. The energy induced in the sub-surface is given by the moment of the integral

$$q = \int_{t=0}^{\tau_p} I(t)t dt, \quad (1)$$

which gives for a rectangular envelope of the pulse of constant $I(t) = I_0$

$$q = I_0 \tau_p. \quad (2)$$

Hence, the total energy emitted by the transmission pulse q is called the *pulse moment*. The component of \mathbf{B}_1 perpendicular to \mathbf{B}_0 imposes a torque on the precessing protons that causes them to tilt away from \mathbf{B}_0 (Fig. 1b). This results in a reduced or zero net spin magnetization parallel to \mathbf{B}_0 and an enhanced net spin magnetization perpendicular to it. Upon switching off the current that generates \mathbf{B}_1 , the parallel (or longitudinal) and perpendicular (or transverse) components of spin magnetization relax exponentially to their original states (Fig. 1c). The precession of the decaying transverse component generates a small but perceptible macroscopic alternating magnetic field that can be detected and measured by the same or a second Faraday loop of wire (the receiver loop) deployed at the surface.

For a single transmission with a fixed pulse moment q , spins in certain regions in the sub-surface are tilted from their equilibrium orientation. Increasing q increases the sub-surface volume within which spins are tilted. Furthermore, spins exposed to relatively strong fields, i.e. close to the loop, are tilted by large amounts, such that they may go through multiple revolutions. In a highly inhomogeneous secondary field the spins that experience multiple revolutions lose coherence and their effects mutually cancel out. Hence, increasing q leads at one hand to a larger volume of investigation and on the other hand to a mask-

ing of NMR signals in strong fields close to the loop. By choosing a suitable series of q values, the water content distribution can be reliably determined for relatively large sub-surface volumes.

During each measurement, the exponentially decaying signal is recorded (Fig. 2, black lines). Single- or multi-exponential decay curves are fitted to the recorded time series (Fig. 2, green lines), which allows the derivation of initial amplitudes V_0 , FID relaxation constants T_2^* and phase lags, ζ , relative to the current in the transmitter [9]. The initial amplitudes V_i are linked quantitatively to the transverse magnetization acquired by the tipping pulse and the number of protons (i.e. water molecules) in the investigated sub-surface volume. From the different time series at increasing q , amplitudes of the complete suite of measurements (red line in Fig. 2) can be used to estimate sub-surface water content.

2.2. The surface NMR signal

The surface NMR signal, induced and recorded by the surface loops, is the superposition of signals from all individual proton spins in the sub-surface. After making the measurements, it is necessary to invert the data in terms of the distribution of spins (i.e. water content). Inversion of the data requires formulations that relate the inducing electromagnetic fields to the NMR-phenomenon. It is particularly important to account for the highly inhomogeneous electromagnetic fields in the sub-surface created by the surface loops.¹ Their orientation and complex field amplitudes throughout the sub-surface depend naturally on the size and shape of the surface loop and distance from

¹ To compute the signal response from a sub-surface volume into the receiver loop, the field of the receiver loop at this sub-surface volume is computed and reciprocity applied. Thus, the *virtual* field of the receiver has to be computed.

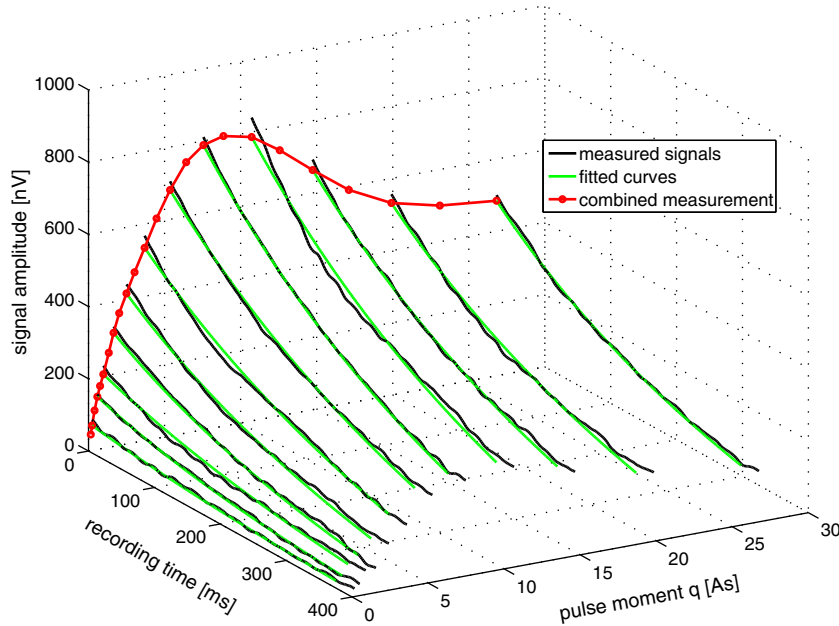


Fig. 2. Data space of a surface NMR measurement. Time series for individual recordings (black lines) are explained by the respective exponential curves (green lines) and initial amplitude V_0 (red line). A suitable suite of pulse moments constitutes a surface NMR measurement curve that can be inverted to provide spatial water content distributions.

the loop but also on the electrical conductivity and magnetic susceptibility distribution of the ground. Within the investigation volume, the fields may (i) vary over orders of magnitude, (ii) be oriented in all directions and (iii) be affected by electromagnetic induction in conductive ground. The latter causes attenuation and elliptical polarization [21] that affects the NMR-phenomenon stronger than the induction-related attenuation. Since the quantitative computation of NMR signal amplitudes in non-homogeneous fields is rarely done (if ever) for conventional NMR applications the derivation is given below.

In its most general form, the surface NMR voltage $V(t)$ is given by:

$$V(t) = - \int d^3\mathbf{r} \int_0^\infty dt' \mathbf{B}_R(\mathbf{r}, t') \cdot \frac{\partial \mathbf{M}}{\partial t}(\mathbf{r}, t - t'), \quad (3)$$

where, \mathbf{B}_R is a virtual magnetic field caused by passing a unit current through the receiver loop and \mathbf{M} is the nuclear magnetization after excitation. The inner integral is the convolution of the temporal variation of spin magnetization with the receiver field as a function of position \mathbf{r} . This represents the contribution of spin magnetization at \mathbf{r} to the total signal. The outer integral is the volume integral over the entire population of contributing spins. Both, \mathbf{B}_R and \mathbf{M} are functions of the time-dependent electromagnetic fields of the surface loops $\mathbf{B}(t)$, acting at \mathbf{r} .

2.2.1. The magnetic fields

To evaluate the integral in Eq. (3), analytic expressions for the interaction of the spins with loop fields $\mathbf{B}_{T,R}$, generated by the transmitter and receiver, respectively, have to be derived. Because spins only absorb and emit energy at

the Larmor frequency ω_L , only this frequency needs to be considered in the computations. Hence, for a more convenient notation, the frequency dependency of the loop magnetic fields and their components as they enter the mathematical description of the surface NMR signal is dropped subsequently.

Of the electromagnetic field $\mathbf{B}_{T,R}(\mathbf{r}, t)$ generated (in reality or virtually) by the surface loops at \mathbf{r} , only the component perpendicular to the local magnetic field of the Earth, $\mathbf{B}_{T,R}^\perp(\mathbf{r})$ interacts with the spin system, where

$$\mathbf{B}_{T,R}^\perp(\mathbf{r}, t) = \mathbf{B}_{T,R}(\mathbf{r}, t) - (\mathbf{b}_0 \cdot \mathbf{B}_{T,R}(\mathbf{r}, t))\mathbf{b}_0. \quad (4)$$

In the following, $\mathbf{b}_{T,R}(\mathbf{r}), \mathbf{b}_{T,R}^\perp(\mathbf{r})$ denote the static unit vectors of the time-dependent fields $\mathbf{B}_{T,R}(\mathbf{r}, t), \mathbf{B}_{T,R}^\perp(\mathbf{r}, t)$, i.e. the unit vectors of the major axis of the polarization ellipse, and \mathbf{b}_0 denotes the unit vector of \mathbf{B}_0 .

For an elliptically polarized excitation field, which is the general case in conductive media, its perpendicular projection \mathbf{B}^\perp is also elliptically polarized unless \mathbf{B}_0 lies in the plane of \mathbf{B} . The projected elliptical field, determined by Eq. (4), can be decomposed into two circular rotating parts that spin clockwise and counterclockwise relative to the spin precession as follows:

$$\begin{aligned} \mathbf{B}_{T,R}^\perp(\mathbf{r}, t) &= \mathbf{B}_{T,R}^+(\mathbf{r}, t) + \mathbf{B}_{T,R}^-(\mathbf{r}, t) \\ &= \left(\alpha_{T,R}(\mathbf{r})\mathbf{b}_{T,R}^\perp(\mathbf{r}) \cos(\omega_L t - \zeta_{T,R}(\mathbf{r})) + \beta_{T,R}(\mathbf{r})\mathbf{b}_0 \right. \\ &\quad \left. \times \mathbf{b}_{T,R}^\perp(\mathbf{r}) \sin(\omega_L t - \zeta_{T,R}(\mathbf{r})) \right), \end{aligned} \quad (5)$$

where $\mathbf{B}_{T,R}^+$ and $\mathbf{B}_{T,R}^-$ are the circularly polarized co- and counter-rotating components of the elliptically polarized vector $\mathbf{B}_{T,R}^\perp$, α and β are the major and minor axes of the

ellipse and ζ is chosen in such a way, that α and β are real. \mathbf{B}^+ and \mathbf{B}^- can be written as

$$\mathbf{B}_{T,R}^{\pm}(\mathbf{r}, t) = \frac{1}{2}(\alpha_{T,R}(\mathbf{r}) \mp \beta_{T,R}(\mathbf{r})) \left(\mathbf{b}_{T,R}^{\pm}(\mathbf{r}) \cos(\omega_L t - \zeta_{T,R}(\mathbf{r})) \mp \mathbf{b}_0 \times \mathbf{b}_{T,R}^{\pm}(\mathbf{r}) \sin(\omega_L t - \zeta_{T,R}(\mathbf{r})) \right), \quad (6)$$

where

$$|\mathbf{B}_{T,R}^{\pm}(\mathbf{r}, t)| = \frac{1}{2}[\alpha_{T,R}(\mathbf{r}) \mp \beta_{T,R}(\mathbf{r})] \quad (7)$$

and the complex unit vectors

$$\mathbf{b}_{T,R}^{\pm}(\mathbf{r}, t) = \frac{\mathbf{B}_{T,R}^{\pm}(\mathbf{r}, t)}{|\mathbf{B}_{T,R}^{\pm}(\mathbf{r}, t)|} \quad (8)$$

$$= \mathbf{b}_{T,R}^{\pm}(\mathbf{r}) \cos(\omega_L t - \zeta_{T,R}(\mathbf{r})) \mp \mathbf{b}_0 \times \mathbf{b}_{T,R}^{\pm}(\mathbf{r}) \sin(\omega_L t - \zeta_{T,R}(\mathbf{r})) \quad (9)$$

$$= \frac{1}{2}[\mathbf{b}_{T,R}^{\pm}(\mathbf{r}) \mp i\mathbf{b}_0 \times \mathbf{b}_{T,R}^{\pm}(\mathbf{r})] e^{-i(\omega_L t - \zeta_{T,R}(\mathbf{r}))} + \text{c.c.}, \quad (10)$$

where c.c. is the complex conjugate of the preceding expression.

2.2.2. The vector spin magnetization

For spin ensembles that generate a macroscopic magnetization $\mathbf{M}(\mathbf{r})$, only an excitational force of a monochromatic field in direction $\mathbf{b}_T^{\pm}(\mathbf{r})$ will force it on a precessional motion in the plane spanned by the vectors $\mathbf{b}_T^{\pm}(\mathbf{r})$ and $\mathbf{b}_0 \times \mathbf{b}_T^{\pm}(\mathbf{r})$. Its oscillation can be described in terms of its spatial components as

$$\mathbf{M}(\mathbf{r}, t) = M(\mathbf{r}) \{ M_{\parallel}(\mathbf{r}) \mathbf{b}_0 + M_{\perp}(\mathbf{r}) [\mathbf{b}_T^{\pm}(\mathbf{r}) \sin(\omega_L t - \zeta_T(\mathbf{r})) + \mathbf{b}_0 \times \mathbf{b}_T^{\pm}(\mathbf{r}) \cos(\omega_L t - \zeta_T(\mathbf{r}))] \}, \quad (11)$$

where $M(\mathbf{r})$ is the spin magnetization at location \mathbf{r} , and M_{\parallel} and M_{\perp} the components of the magnetic moment oriented in the directions of the static field \mathbf{B}_0 and perpendicular to it, respectively. Only M_{\perp} oscillates and, consequently, emits an electromagnetic signal. The time derivative of $\mathbf{M}(\mathbf{r}, t)$ in Eq. (3) is

$$\partial_t \mathbf{M}(\mathbf{r}, t) = \omega_L M(\mathbf{r}) M_{\perp}(\mathbf{r}) \times [\mathbf{b}_T^{\pm}(\mathbf{r}) \cos(\omega_L t - \zeta_T(\mathbf{r})) - \mathbf{b}_0 \times \mathbf{b}_T^{\pm}(\mathbf{r}) \sin(\omega_L t - \zeta_T(\mathbf{r}))]. \quad (12)$$

Clearly, only the term in brackets of the second line of Eq. (12) contributes. The expression in the brackets of Eq. (12) is the unit co-rotating part of the transmitter field in Eq. (9). Hence, Eq. (12) simplifies to

$$\partial_t \mathbf{M}(\mathbf{r}, t) = \omega_L M(\mathbf{r}) M_{\perp}(\mathbf{r}) \mathbf{b}_T^{\pm}(\mathbf{r}, t). \quad (13)$$

This explicitly demonstrates that the spin magnetization $\mathbf{M}(\mathbf{r}, t)$, created by the co-rotating part of the tipping pulse, oscillates in a fixed direction and with fixed phase relative to the transmitter field.

2.2.3. The NMR signal for surface loops

With the expressions for the magnetic field components and the spin magnetization, the expression for the surface

NMR signal can now be quantitatively evaluated. Substituting Eq. (13) into Eq. (3) and including the spatial aspects yields

$$V(t) = -\omega_L \int d^3 r M(\mathbf{r}) M_{\perp}(\mathbf{r}) \int_0^{\infty} dt' \mathbf{B}_R(\mathbf{r}, t') \mathbf{b}_T^{\pm}(\mathbf{r}, t - t'). \quad (14)$$

By substituting the complex expression for $\mathbf{b}_T^{\pm}(\mathbf{r}, t)$ from Eq. (10), Eq. (14) becomes

$$V(t) = -\omega_L \int d^3 r M(\mathbf{r}) M_{\perp}(\mathbf{r}) \int_0^{\infty} dt' \mathbf{B}_R(\mathbf{r}, t') \times \frac{1}{2} [(\mathbf{b}_T^{\pm}(\mathbf{r}) - i\mathbf{b}_0 \times \mathbf{b}_T^{\pm}(\mathbf{r})) e^{-i(\omega_L(t-t') - \zeta_T(\mathbf{r}))} + \text{c.c.}]. \quad (15)$$

Rewriting the exponential expression $e^{-i(\omega_L(t-t') - \zeta_T(\mathbf{r}))}$ as $e^{-i\omega_L t} e^{i\omega_L t'} e^{i\zeta_T(\mathbf{r})}$, Eq. (15) can be rearranged to

$$V(t) = -\frac{1}{2} \omega_L \int d^3 r M(\mathbf{r}) M_{\perp}(\mathbf{r}) \times \left\{ \left[e^{i\zeta_T(\mathbf{r})} (\mathbf{b}_T^{\pm}(\mathbf{r}) - i\mathbf{b}_0 \times \mathbf{b}_T^{\pm}(\mathbf{r})) e^{-i(\omega_L t)} \times \int_0^{\infty} dt' \mathbf{B}_R(\mathbf{r}, t') e^{i\omega_L t'} \right] + \text{c.c.} \right\}. \quad (16)$$

The integral in the third line simply represents a Fourier-integral that transforms the causal time-dependent field amplitude $\mathbf{B}_R(\mathbf{r}, t')$ into a frequency dependent one $\mathbf{B}_R(\mathbf{r})$,² so that the expression can be changed into

$$V(t) = -\frac{1}{2} \omega_L \int d^3 r M(\mathbf{r}) M_{\perp}(\mathbf{r}) \times e^{i\zeta_T(\mathbf{r})} [\mathbf{b}_T^{\pm}(\mathbf{r}) - i\mathbf{b}_0 \times \mathbf{b}_T^{\pm}(\mathbf{r})] e^{-i(\omega_L t)} \times (\mathbf{B}_R(\mathbf{r}, t) + \text{c.c.}). \quad (17)$$

The vector \mathbf{B}_R is multiplied by the static unit vectors \mathbf{b}_T^{\pm} and $\mathbf{b}_0 \times \mathbf{b}_T^{\pm}$ in the plane normal to \mathbf{B}_0 , so that all components of \mathbf{B}_R parallel to \mathbf{B}_0 vanish and only the perpendicular component of \mathbf{B}_R is physically meaningful. Thus, \mathbf{B}_R can be conveniently replaced by \mathbf{B}_R^{\perp} . Using the relationships provided by Eq. (5), Eq. (17) becomes

$$V(t) = -\frac{1}{2} \omega_L \int d^3 r M(\mathbf{r}) M_{\perp}(\mathbf{r}) \times \left\{ e^{i\zeta_T(\mathbf{r})} [\mathbf{b}_T^{\pm}(\mathbf{r}) - i\mathbf{b}_0 \times \mathbf{b}_T^{\pm}(\mathbf{r})] e^{-i(\omega_L t)} \times e^{i\zeta_R(\mathbf{r})} [\alpha_R(\mathbf{r}) \mathbf{b}_R^{\perp}(\mathbf{r}) + i\beta_R(\mathbf{r}) \mathbf{b}_0 \times \mathbf{b}_R^{\perp}(\mathbf{r})] + \text{c.c.} \right\}. \quad (18)$$

Commonly the positive envelope of the signal is determined, digitally or by hardware filters [9]. This results in the effect of the Larmor frequency oscillations being removed, such that the signal simplifies to its real and imaginary envelopes:

$$V_0 = -\omega_L \int d^3 r M(\mathbf{r}) M_{\perp}(\mathbf{r}) \times e^{i\zeta_T(\mathbf{r})} [\mathbf{b}_T^{\pm}(\mathbf{r}) - i\mathbf{b}_0 \times \mathbf{b}_T^{\pm}(\mathbf{r})] \times e^{i\zeta_R(\mathbf{r})} [\alpha_R(\mathbf{r}) \mathbf{b}_R^{\perp}(\mathbf{r}) + i\beta_R(\mathbf{r}) \mathbf{b}_0 \times \mathbf{b}_R^{\perp}(\mathbf{r})]. \quad (19)$$

² As for all other parameters $\mathbf{B}_R(\mathbf{r}, \omega)$ acts only at ω_L , the frequency is dropped for a more convenient notation.

By carrying out the multiplications and rearranging, Eq. (19) can be rewritten as

$$V_0 = -\omega_L \int d^3r M(\mathbf{r}) M_{\perp}(\mathbf{r}) \times [\alpha_{\mathbf{R}}(\mathbf{r}) + \beta_{\mathbf{R}}(\mathbf{r})] \cdot e^{i[\zeta_{\mathbf{T}}(\mathbf{r}) + \zeta_{\mathbf{R}}(\mathbf{r})]} \times [\mathbf{b}_{\mathbf{R}}^{\perp}(\mathbf{r}) \cdot \mathbf{b}_{\mathbf{T}}^{\perp}(\mathbf{r}) + i\mathbf{b}_0 \cdot \mathbf{b}_{\mathbf{R}}^{\perp}(\mathbf{r}) \times \mathbf{b}_{\mathbf{T}}^{\perp}(\mathbf{r})]. \quad (20)$$

Here, M_{\perp} can be expressed by the approximation for the spin perturbation [22]

$$M_{\perp} = \sin(\Theta_{\mathbf{T}}) = \sin(-\gamma q | \mathbf{B}_{\mathbf{T}}^+(\mathbf{r}) |), \quad (21)$$

where $\Theta_{\mathbf{T}}$ denotes the spin tipping angle. The tipping angle is determined by the spin nutation $\sin(-\gamma | \mathbf{B}_{\mathbf{T}}^+(\mathbf{r}) |)$, scaled by the pulse moment q .

The expression in brackets in the second line of Eq. (20) is the absolute value of the counter-rotating part of the receiver field in Eq. (7). Furthermore, the magnetization $M(\mathbf{r})$ is the spin magnetization of the investigated water protons, which can be represented as the product of the specific magnetization of hydrogen protons M_0 and the water content $f(\mathbf{r})$

$$M(\mathbf{r}) = 2M_0 f(\mathbf{r}). \quad (22)$$

The factor of two arises from the chemistry of the water molecule containing two hydrogen protons. Substituting the identities from Eqs. (21) and (22) into Eq. (20) yields the formulation of the surface NMR initial amplitudes as introduced by Weichman et al. [16]:

$$V_0(q) = 2\omega_L M_0 \int d^3r f(\mathbf{r}) \sin(-\gamma q | \mathbf{B}_{\mathbf{T}}^+(\mathbf{r}) |) \times | \mathbf{B}_{\mathbf{R}}^-(\mathbf{r}, t) | \cdot e^{i[\zeta_{\mathbf{T}}(\mathbf{r}) + \zeta_{\mathbf{R}}(\mathbf{r})]} \times [\mathbf{b}_{\mathbf{R}}^{\perp}(\mathbf{r}) \cdot \mathbf{b}_{\mathbf{T}}^{\perp}(\mathbf{r}) + i\mathbf{b}_0 \cdot \mathbf{b}_{\mathbf{R}}^{\perp}(\mathbf{r}) \times \mathbf{b}_{\mathbf{T}}^{\perp}(\mathbf{r})]. \quad (23)$$

2.2.4. Isolating the integral kernel

The general forward functional of Eq. (23), can be expressed as an integral with the water content distribution $f(\mathbf{r})$ as the dependent parameter and a general data kernel $K(q, \mathbf{r})$:

$$V_0(q) = \int K(q, \mathbf{r}) f(\mathbf{r}) d\mathbf{r}, \quad (24)$$

with

$$K(q, \mathbf{r}) = 2\omega_L M_0 \sin(-\gamma q | \mathbf{B}_{\mathbf{T}}^+(\mathbf{r}) |) \times | \mathbf{B}_{\mathbf{R}}^-(\mathbf{r}) | \cdot e^{i[\zeta_{\mathbf{T}}(\mathbf{r}) + \zeta_{\mathbf{R}}(\mathbf{r})]} \times [\mathbf{b}_{\mathbf{R}}^{\perp}(\mathbf{r}) \cdot \mathbf{b}_{\mathbf{T}}^{\perp}(\mathbf{r}) + i\mathbf{b}_0 \cdot \mathbf{b}_{\mathbf{R}}^{\perp}(\mathbf{r}) \times \mathbf{b}_{\mathbf{T}}^{\perp}(\mathbf{r})]. \quad (25)$$

This data kernel contains measurement-configuration-dependent information (e.g. loop configuration), the magnitude and inclination of the local Earth magnetic field, pulse moment series, sub-surface resistivity distribution (contained in $\mathbf{B}_{\mathbf{T},\mathbf{R}}$) and the various physical constants. It is calculated for each measurement configuration and pulse series. The spatial distributions of the electromagnetic fields generated and received by the surface loops are calculated for conducting ground using Debye potentials in the spatial wave-number domain and then transferred to the

space domain (e.g. [23]). The sub-surface resistivity distribution has to be known a priori and is usually assumed to be independent of the water content distribution.

In Eq. (23), the magnetic field components of the transmitter and receiver loops are represented only by their co- and counter-rotating parts, respectively. The fact that the counter-rotating part of the receiver field enters the equation is a consequence of the reciprocity of mutual induction between the loop and the spin magnetization.

The three lines of Eq. (23) can be interpreted as follows:

- (1) The first line contains the signal amplitude of the spin system emitting the NMR response. It includes the water content term $f(\mathbf{r})$ and the sinusoid of the tip angle, which is determined by the pulse moment q and the normalized amplitude of the co-rotating part of the transmitter field.
- (2) The second line describes the sensitivity of the receiver loop to a signal in the sub-surface; it is independent of the excitation intensity. It is a function of the hypothetical magnetic field distribution associated with the receiver loop and phase lags caused by electromagnetic attenuation.
- (3) The final line accounts for the possible separation of the transmitter and receiver loops. Whereas the first two lines contain scalar quantities, this one includes information on the vectorial evolution of the magnetic fields and is generally complex-valued. The resulting phase shift, which is due to the geometry of the entire system, is in addition to phase phenomena associated with (i) excitation pulses off the Larmor frequency, (ii) signal propagation in conductive media and (iii) hardware related phases, e.g. resonant circuits for the receiver loop.

3. Inversion of surface NMR data

Inversion techniques are required to derive models of sub-surface water content from single or multiple surface NMR measurements. Whereas most NMR imaging methods produce highly spatially selective data, the surface NMR techniques is rather integrative. Each measurement at a specific pulse moment q senses large regions of the sub-surface at individual sensitivity. From a series of measurements at varying pulse moments, that provide a suitable coverage, a spatially resolved water content model can be obtained. Thus, models that explain the data in a best-fit sense have to be determined, usually by incorporating a priori model constraints.

Inversion is not a simple turnkey operation but generally requires individually adopted processing steps which in turn requires a basic understanding of inversion principles. The layered model, the style of model discretization, the a priori information and the actual inversion scheme all have a marked influence on the inversion result. Additionally, the derived models are neither exact nor unique

within the finite measurement accuracies. In the following the basic inverse formulations for surface NMR data are derived and applied to 1-D and 2-D synthetic data. For the 1-D examples, two different, but complementary approaches are discussed in more detail.

The forward problem is given by Eqs. (23)–(25). Eq. (23) is a common Fredholm integral equation of the first kind, a form that is quite common in geophysical inverse methods [24]. Evaluating the integral in Eq. (23) for a range of q_i values yields a suite of readings $V_i = V(q_i)$

$$V_i = \int K_i(\mathbf{r})f(\mathbf{r})d\mathbf{r}, \quad (26)$$

with $i = 1, 2, \dots, N_q$ the number of pulse moments for a complete measurement. Further discretization in the space domain allows appropriate numerical modeling methods to be employed. By approximating the continuous water content to be piecewise constant for intervals $\Delta\mathbf{r}$, Eq. (26) becomes

$$V_i \approx \sum K_i(\mathbf{r}_j)f(\mathbf{r}_j)\Delta\mathbf{r}_j, \quad (27)$$

where $j = 1, 2, \dots, N_r$ is the number of discretized spatial elements. Values for $K_i(\mathbf{r}_j)$ have to be determined either by a simple quadrature rule or by more accurate numerical integration, depending on the size of the discretization steps. The system of equations in Eq. (27) can be conveniently written in matrix notation as

$$\mathbf{V} = \mathbf{K}\mathbf{f}, \quad (28)$$

with the dimensions of the matrices as follows: $\mathbf{V} : 1 \times N_q$, $\mathbf{K} : N_q \times N_r$ and $\mathbf{f} : N_r \times 1$.

The aim of inversion is to determine a sub-surface water content model that explains the surface NMR measurements as follows:

$$\mathbf{f} = \mathbf{K}^{-1}\mathbf{V}. \quad (29)$$

This problem is ill-conditioned and ill-posed in most cases. It cannot be solved directly.

Several schemes for solving the surface NMR inverse problem have been published [10,25–29]. They include approaches based on models with fixed and variable geometry and different means of seeking optimum solutions (e.g. linearized least-squares, Monte-Carlo, simulated annealing). The following schemes employ least-squares techniques, which are very common in geophysics.

3.1. 1-D investigations: magnetic resonance sounding (MRS)

In standard 1-D investigations, the sub-surface is assumed to be horizontally stratified and the water content to vary only with depth. Measurements are performed using the deployment of a single loop that generates the pulse and records the resultant NMR signal. The characteristics of this measurement configuration to achieve increasing depth penetration depth with increasing q is the basis for the name “(depth) sounding”.

For this 1-D problem using the coincident loop configuration, $\mathbf{b}_T(\mathbf{r})$ and $\mathbf{b}_R(\mathbf{r})$ are identical such that Eq. (23) simplifies to

$$K(q, \mathbf{r}) = -2\omega_L M_0 \sin(-\gamma q |\mathbf{B}^+(\mathbf{r})|) \times |\mathbf{B}^-(\mathbf{r})| \cdot e^{i2\zeta(\mathbf{r}, \omega_L)}. \quad (30)$$

Writing the general forward problem from Eq. (30) in Cartesian coordinates:

$$V_i = \int_0^\infty \int_{-\infty}^{+\infty} \int_{-\infty}^{+\infty} K_i(x, y, z)f(x, y, z) dx dy dz, \quad (31)$$

and assuming laterally homogeneous water content

$$\frac{\partial f(x)}{\partial x} = \frac{\partial f(y)}{\partial y} = 0, \quad (32)$$

the data kernel $K_i(x, y, z)$ can be pre-integrated in both horizontal dimensions x and y to give

$$K_{i,1D}(z) = \int_{-\infty}^{+\infty} \int_{-\infty}^{+\infty} K_i(x, y, z) dx dy. \quad (33)$$

Thus, the forward problem to compute a series of synthetic measurements V_i from a known water content model $f(z)$ is given by

$$V_i = \int_0^\infty K_i(z)f(z) dz. \quad (34)$$

Here, the data kernel and water content are continuous functions with depth. To determine a 1-D water content model we review two inversion schemes: one that assumes a large number of layers with fixed boundaries and then determines the water content in each layer, and the other that determines thicknesses and water contents of a few layers.

3.1.1. Fixed geometry inversion

For fixed geometry inversions, the models are defined by many layers with fixed (and known) boundaries. Only the water content in each layer is allowed to vary during the inversions. The water content distribution \mathbf{f} is therefore the only dependent variable of the forward problem. From Eq. (28), we see that for a measurement, the surface NMR signal \mathbf{V} is linearly related to the water content distribution \mathbf{f} , such that the kernel \mathbf{K} is the sensitivity or Jacobian matrix of the inverse problem. The data functional to be minimized by least-squares analysis is

$$\Phi_d(\mathbf{V}) = \sum_{i=1}^P \left| \frac{V_i - K_{ij}f_i}{\epsilon_i} \right|^2 = \|\mathbf{D}(\mathbf{V} - \mathbf{K}\mathbf{f})\|_2^2, \quad (35)$$

where misfits between the measured data V_i and model-predicted data $K_{ij}f_i$, based on water content estimates f_i , are weighted by their errors ϵ_i , which is equivalent to the data weighting matrix \mathbf{D} . As in many geophysical applications, the number of layers required to provide sufficient resolution (i.e. the number of model parameters), often exceeds the number of data points. Consequently,

the system of equations is under-determined, such that additional model constraints are required. Plausible model constraints include demanding the model to be simple (damping) by minimizing the Euclidean length of the model parameters $\mathbf{f}^T \mathbf{f}$, or demanding minimum variations between adjacent model parameters (smoothing) by applying Tikhonov regularization [24]. The model functional then gives

$$\Phi_m(\mathbf{f}) = \|\mathbf{C}_m \mathbf{f}\|_2^2, \quad (36)$$

where \mathbf{C}_m is the a priori model covariance matrix, that contains the appropriate model constraint. The complete functional to be minimized is given by

$$\Phi = \Phi_d + \lambda \Phi_m \rightarrow \min, \quad (37)$$

with λ a regularization weighting factor (also known as trade-off or damping factor).

The system of equations to be solved is linear and could be solved in a direct fashion. Unfortunately, such inversions may result in ridiculous results with $f > 100\%$ or $f < 0\%$ water content estimates. To avoid these patterns, it is necessary to apply constraints on the range of water content. Constraining the water content in the inversion scheme by modifying the Jacobian matrix changes the system to be slightly non-linear, thus requiring an iterative approach. Starting from an arbitrary initial model, the model vector is updated during the l th iteration by

$$\mathbf{f}^{l+1} = \mathbf{f}^l + v^l \Delta \mathbf{f}^l, \quad (38)$$

where v^l is the line search parameter. The model update $\Delta \mathbf{f}^l$ is determined by solving the Gauss–Newton system of equations [30]

$$\Delta \mathbf{f}^l = (\mathbf{K}^T \mathbf{C}_d^{-1} \mathbf{K} + \lambda \mathbf{C}_m^{-1}) (\mathbf{K}^T \mathbf{C}_d^{-1} (\mathbf{V} - \mathbf{K} \mathbf{f}^{l-1}) - \lambda \mathbf{C}_m^{-1} \mathbf{f}^{l-1}), \quad (39)$$

where $\mathbf{C}_m^{-1} = \mathbf{C}_m^T \mathbf{C}_m$ and $\mathbf{C}_d^{-1} = \mathbf{D}^T \mathbf{D}$ are the model and data covariances. Fig. 3a shows surface NMR data for a simple three layer model in which water content is significantly higher in the middle layer. The true model is shown in Fig. 3b by the gray line. To simulate realistic conditions, 10 nV Gaussian noise (corresponding to about 5% of the simulated data with median amplitudes of some 200 nV) is added to the data. Application of the fixed geometry inversion scheme produces the smooth model, represented by the dashed line in Fig. 3b. Although the principal features of the true model are reproduced by this inversion, the smoothness constraints lead to “smearing” of the layer boundaries and a slight overestimation of the maximum water content within the second layer. The advantages of the fixed geometry inversion scheme is that no a priori information is required and even complex models with an unknown number of layers or smooth water content variations can be reliably reconstructed. However, accurate derivations of layer boundaries and water contents may be systematically limited by this approach.

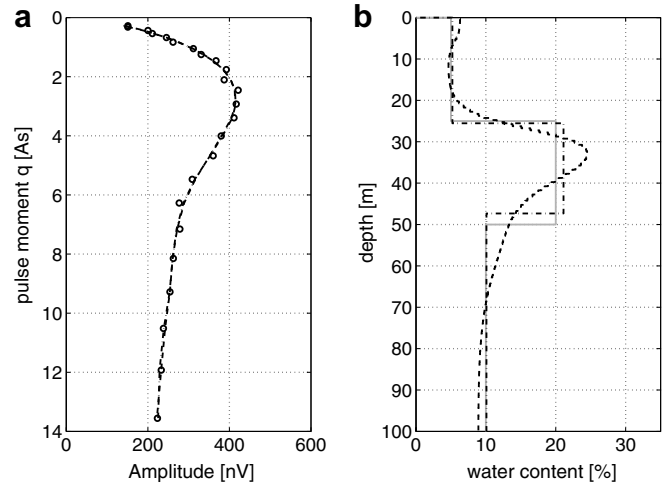


Fig. 3. Comparison of the two inversion schemes: one with fixed geometry of numerous layers in which the water content of each layer is allowed to vary and one with three layers in which the layer boundaries and water content are allowed to vary. The true model (gray line in (b)) was used to generate a synthetic data set affected by 10 nV of Gaussian noise (circles in (a)). Inversion using the fixed-boundary approach and smoothness constraints on the model yields a reasonable model of water content (dashed in (b)), but with both boundaries smoothed rather than sharp and the maximum water content of the middle layer is slightly overestimated. Inversion for variable three layer model (dash-dotted in (b)) accurately represents all important details of the true model. Both models fit the data equally well.

3.1.2. Variable geometry inversion

The variable geometry inversion scheme is based on the assumption that sub-surface water content can be represented by a small number of discrete boundaries and water contents of which can be determined during the inversion process. Such a scheme is useful if geological or other a priori information indicates that simple layered models are appropriate representations of the sub-surface.

Assuming that three layers with water contents $f = [f_1, f_2, f_3]^T$ and depths $z = [0, z_1, z_2, z_{\max}]$ are sufficient, then Eq. (34) can be rewritten as

$$V_i = \int_0^{z_1} K_i(z) f_1(z) dz + \int_{z_1}^{z_2} K_i(z) f_2(z) dz + \int_{z_2}^{z_{\max}} K_i(z) f_3(z) dz. \quad (40)$$

The Jacobian matrix of this forward operator in respect to the water content f is given by

$$G_{ij}^f = \frac{\partial V_i}{\partial f_j} \quad (41)$$

$$= \left[\int_0^{z_1} K_i(z) dz, \int_{z_1}^{z_2} K_i(z) dz, \int_{z_2}^{z_{\max}} K_i(z) dz \right]^T \quad (42)$$

$$= [K1_i, K2_i, K3_i]^T, \quad (43)$$

where $K1_i, K2_i, K3_i$ are rows of the Jacobian denoting the sensitivity of the solution to the water contents in the respective layers. Determining the Jacobian for the layer boundaries z_1, z_2 yields

$$G_{ij}^z = \frac{\partial V_i}{\partial z_j} \quad (44)$$

$$= [(f_2 - f_1)K_i(z_1), (f_3 - f_2)K_i(z_2)]^T. \quad (45)$$

The total Jacobian matrix is then given by

$$G_{ij} = [G_{ij}^z, G_{ij}^f]^T \quad (46)$$

$$= [K1_i, K2_i, K3_i, (f_2 - f_1)K_i(z_1), (f_3 - f_2)K_i(z_2)]^T. \quad (47)$$

For surface NMR inversion with variable boundaries, the matrix entries for the depths are dependent on the water contents of the respective layers. Thus, the inversion is in general non-linear and has to be solved in an iterative fashion. The inverse problem can then be written as [24]

$$\Delta \mathbf{f}_l = [\mathbf{G}_l^T \mathbf{C}_d^{-1} \mathbf{G}_l + \lambda \mathbf{C}_m^{-1}]^{-1} \mathbf{G}_l^T (\mathbf{V} - \mathbf{K} \mathbf{f}_{l-1}), \quad (48)$$

where $\Delta \mathbf{f}_l$ is the model update for the l th iteration, \mathbf{C}_m^{-1} and \mathbf{C}_d^{-1} are again the model and data covariances, λ is the regularization factor and $(\mathbf{V} - \mathbf{K} \mathbf{f})$ are the residuals of the measured data \mathbf{V} and the water model \mathbf{f}_{l-1} from the $l - 1$ st iteration. For the given inversion scheme, the number of data points is larger than the number of model parameters. Thus, no additional model constraints need to be applied. However, constraint matrices \mathbf{C}_m and/or \mathbf{C}_d should be implemented to avoid a badly conditioned inverse of $[\mathbf{G}^T \mathbf{G}]$ and therefore stabilize the inversion.

Application of the variable geometry inversion using three layers to the synthetic data of Fig. 3a yields a near-perfect reconstruction of the true model (black dash-dotted line in Fig. 3b), compared to the initial model (gray line). Clearly this inversion scheme is capable of providing highly accurate results as long as there are a limited number of discrete layers and the number of layers is known beforehand. Of course, if the number of layers is unknown and/or the boundaries are gradational rather than sharp, the results of applying the variable-boundary scheme will be flawed.

3.1.3. Reliability of water content estimates

The reliability of the sub-surface water content model depends on the data quality. Usually, a range of models can be found that explain the observed data equally well within the measurement errors. Inversion may yield the model with the closest fit to the data, but other models with quite different parameters might be just as valid. In addition to determining the best-fit model, estimating its reliability and evaluating model ambiguity are important components of a surface NMR investigation.

For linear problems and for data contaminated by Gaussian distributed noise, model uncertainty can be estimated from the model covariances [31]. In surface NMR, the inverse problem is non-linear and the measurements can include both Gaussian noise and non-Gaussian measurement errors. A powerful tool for estimating model uncertainty in this case is the method of bootstrap resampling [32], based on studentized residuals.³ Bootstrapping

is the practice of estimating median values and standard deviations of the model when measuring those properties when sampling from an approximating distribution of the data.

For a bootstrap analysis probability density functions (PDF) for each data point are determined, with the data point itself as a mean value and the residuals of the measured data and data predicted from a best-fit model as the standard deviation. In a next step, numerous replicas of the measured data set are then generated with random numbers for each data point within its PDF. Thus, inversion of the replicated data sets yields a suite of models that all explain the measured data within their measurement accuracy. Variations in the model parameters can be analyzed, thus providing the median values and the standard deviations of model parameters.

For a more robust delineation of outliers *studentized* residuals are usually employed. These are the residuals of the measured data and data predicted from a best-fit model weighted by their individual importance [31]. As an alternative, studentized residuals can be determined by repeating the inversion by the number of data points and determine the residual of each data point with respect to the model built after discarding this observation from the data set.

Fig. 4 shows the result of applying a bootstrap analysis to the simulated data of Fig. 3a. Studentized residuals based on the best-fit model were used to generate 32 replica data sets, which were then inverted. From the resultant suite of models (gray lines in Fig. 4), median model parameters (dashed line in Fig. 4) and their standard deviations (dash-dotted lines in Fig. 4) were computed (Table 1).

The bootstrap analysis demonstrates that the upper boundary of the high water content layer occurs at $25.5 \text{ m} \pm 1 \text{ m}$ (true value 25 m), whereas the lower boundary is less well resolved at $49.7 \text{ m} \pm 4.8 \text{ m}$ (true value 50 m). The water contents of the three layers were deter-

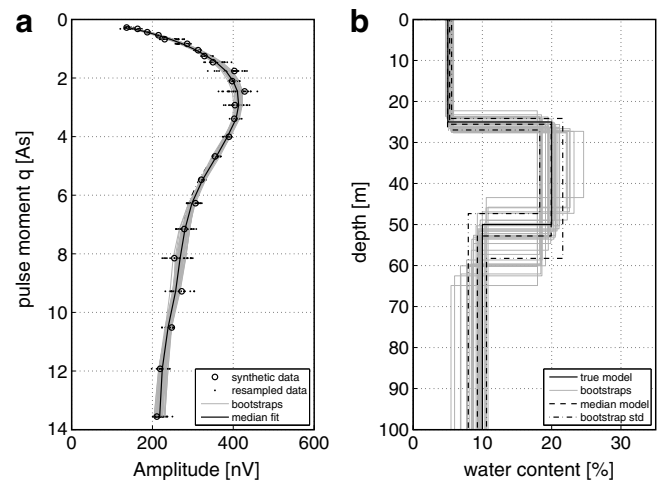


Fig. 4. Results of applying a bootstrap analysis to the same data as shown in Fig. 3. A model with variable geometry was used for the inversion.

³ As their name implies, studentized residuals follow Student's t distributions.

Table 1
Results of the bootstrap analysis for the noise-contaminated three layer data set in Fig. 4 based on 32 inversions of the resampled data

	True values	Median model $\bar{\mu}$	Standard deviation σ
f_1	5%	4.8%	0.2%
f_2	20%	20.1%	1.5%
f_3	10%	10.1%	0.9%
z_1	25 m	25.5 m	1.0 m
z_2	50 m	49.7 m	4.8 m

mined to variable degrees of accuracy with the error for the middle layer being the highest.

3.2. 2-D investigations: magnetic resonance tomography (MRT)

At locations where water content varies laterally, 2-D or 3-D data acquisition and inversion are required. Examples for these structures are isolated groundwater occurrences, called perched water lenses, or water-filled caverns or cavities like Karst structures. For 2-D situations in which water content is a function of x (profile direction) and z (depth), but not the y -coordinate, Eq. (33) becomes

$$K_{i,2-D}(x, z) = \int_{-\infty}^{+\infty} K_i(x, y, z) dy \tag{49}$$

and Eq. (34) becomes

$$V_i = \int_0^{\infty} \int_{-\infty}^{\infty} K_i(x, z) f(x, z) dx dz. \tag{50}$$

Individual values are thus determined by multiplying the 2-D water content distribution with a 2-D data kernel.

To acquire information to estimate 2-D distributions of water content requires measurements along the profile. For this purpose, a coincident transmitter–receiver loop can be incrementally shifted along the profile and/or separate transmitter and receiver loops can be moved systematically relative to each other along the profile. Separate loop measurements provide additional spatial sensitivity, in particular for the shallow sub-surface [18,19].

Fig. 5 displays the effective sensitivities for a coincident loop and three separate loop configurations for three typical pulse moments and for the sum of 16 pulse moments. Increasing the pulse moments for coincident loops (left column) simply increases the probed volume. By contrast, varying the loop separation provides increased sensitivities at shallow depth below the receiver loop. Consequently, by acquiring data using a range of pulse moments and variable transmitter–receiver loop separation, it is possible to increase depth (volume) penetration and sensitivity to lateral changes in the shallow sub-surface.

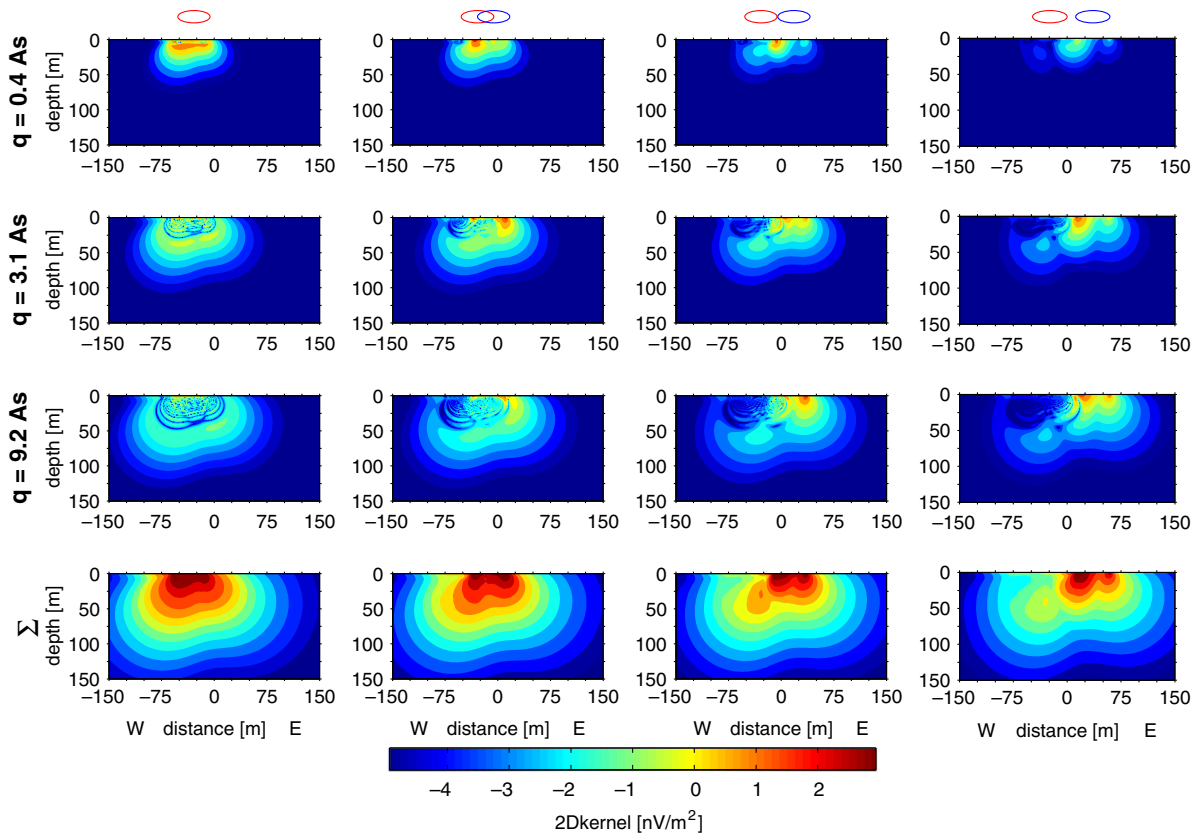


Fig. 5. Contour representation of 2-D data kernels for a coincident-loop configuration (left column) and for configurations with three different loop separations (middle and right columns; see sketches shown to the top of the figure). The first three rows show the sensitivities for three selected pulse moments, the bottom row shows the sum of all 16 pulse moments for a typical measurement. Data kernels are calculated for: Earth’s magnetic field intensity $B_0 = 48,000$ nT, inclination $I = 60^\circ$, azimuth -45° , half-space resistivity $-100 \Omega\text{m}$.

High sensitivities may extend well outside of the loop boundaries. For separate loop measurements the sensitivities are in general non-symmetric and are confined to small volumes below the receiver loop. Additional asymmetry, including measurements in a coincident loop configuration, is a result of the dipping (dipolar) nature of the Earth’s field or may be caused by induction effects that lead to asymmetric splitting of \mathbf{B}_T^+ and \mathbf{B}_R^- in Eq. (23) [19]. Consequently, the distance and orientation of an isolated volume of water relative to the data acquisition loops affect the amplitude versus pulse moment curves.

Inversion of data acquired along a profile using coincident and/or separate loops along a profile yields 2-D water models. The principles of 2-D inversion or magnetic resonance tomography (MRT), are essentially the same as those described for 1-D inversion in Section 3.1. The data kernels for the measurements are determined by Eq. (49), and the 2-D sub-surface models are represented by a grid of water content values.

The influence of the perched water lens in Fig. 6 on a series of coincident loop measurements made along a profile is shown in Fig. 7. The background water content is 5%

by volume, whereas the water content within the lens is 25%. For the four loop positions P1–P4, two series of synthetic measurements are simulated: one for the true 2-D water lens model (solid lines in Fig. 7) and one for the laterally homogeneous 1-D case with layer thicknesses and water contents equal to those of the water content model vertically below the coil centers. For P1 and P4, the water content beneath the coil center is uniformly 5%. However, the loop with a radius of 24 m extends partly across the 2-D lens at these locations and is thus affected by its anomalous water content. At P2 and P3, the loop is entirely across the lens. Comparison of data simulated for the simplified 1-D and full 2-D models demonstrates the strong influence of the perched water lens (Fig. 7). At P1 and P4, synthetic data have lower amplitudes for the simplified 1-D assumption (neglecting the lens) than for the true 2-D model. At P2 and P3, the reversed pattern are found. The asymmetry of the simulated 2-D data is again the result of the Earth’s magnetic field being inclined.

The result of applying the fixed geometry 1-D inversion algorithm to the 2-D synthetic data (i.e. solid lines) of Fig. 7 are presented in Fig. 8. Differences between the left

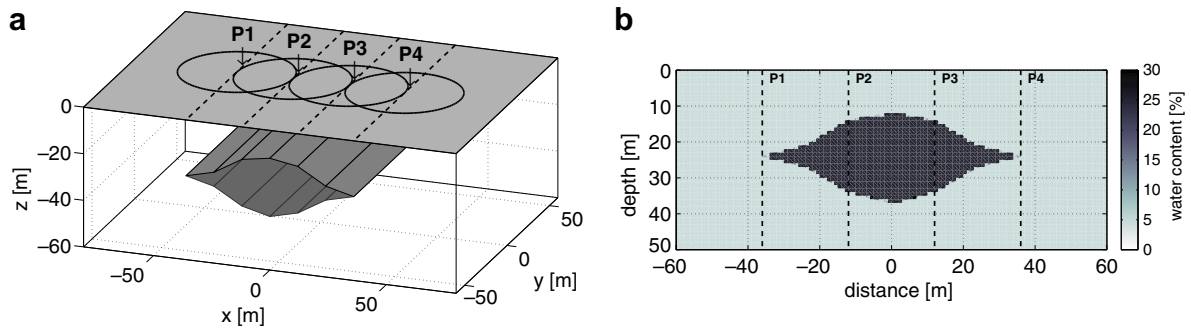


Fig. 6. Sketch of a 2-D model of a perched water-lens model (gray object) and the locations of four synthetic coincident transmitter/receiver coil measurements (black loops in (a)) centered along lines P1–P4. Coil center increment is 24 m and the diameter of the 2 turn coil is 48 m (i.e. 50% overlap between coils). Water content in the lens is 25% by volume and that of the surroundings is 5%. Synthetic data shown in Fig. 7 are calculated for: maximum pulse moments – 10 As, Earth’s magnetic field intensity B_0 – 48,000 nT, inclination I – 60°, azimuth – 45°; half-space resistivity ρ – 100 Ω m.

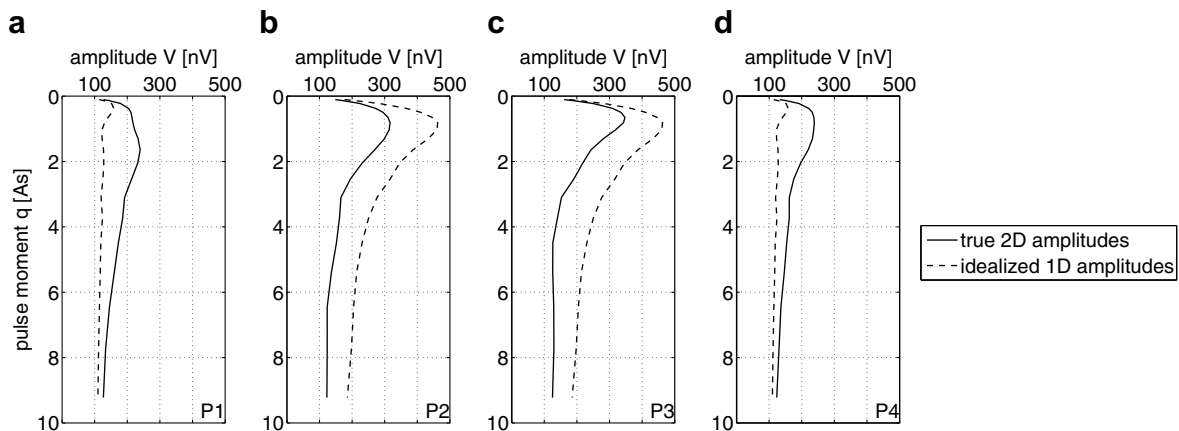


Fig. 7. (a–d) Synthetic surface NMR amplitudes at positions P1–P4 in Fig. 6. Dashed lines are the signals for 1-D models with water content distributions equal to those of the 2-D model vertically below the respective coil centers. Solid lines are the signals for the 2-D water-lens model. Note, that the 2-D synthetic measurements are not symmetric about the center of the lens; the oblique inclination of the Earth’s magnetic field results in asymmetry of the 2-D kernel.

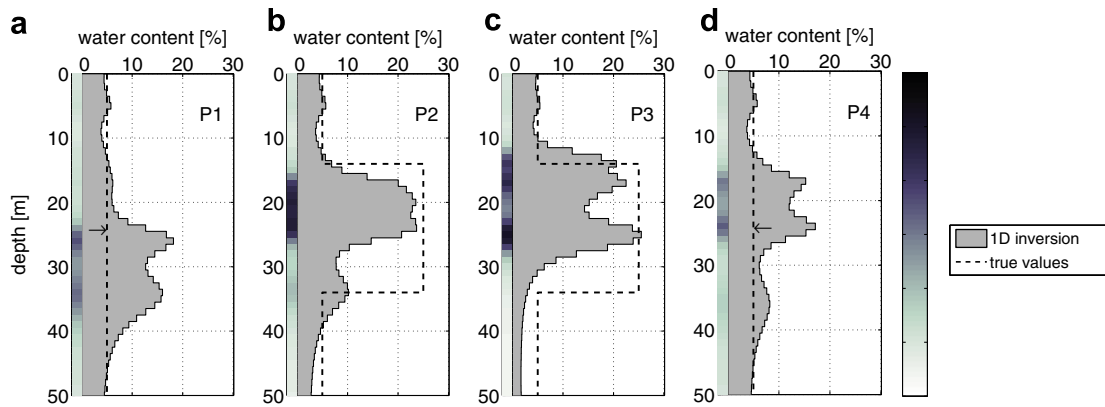


Fig. 8. 1-D inversion results of the four synthetic measurements P1–P4 (solid lines in Fig. 7). Results are shown for a fixed-boundary least-squares inversion (gray areas and color bars). Dashed black lines show the true water content directly below the coil centers. There is no anomalous concentration of water directly below the centers of coils P1 and P4 (see Fig. 6); the apices of the lens at these locations are delineated by arrows in (a) and (d). (For interpretation of the references to color in this figure legend, the reader is referred to the web version of this article.)

and right pairs of models reflect the asymmetries in the 2-D data. All inversion results correctly predict the 5% water content above the lens and good estimates of the depth of the top of the lens are provided at P2 and P3. For loop positions P1 and P4 the inversions overestimate the volume of water immediately below the loop center. At P2 and P3, the depths to the lens' lower boundary, its total water content, and water content below the lens are significantly underestimated. From these results, we conclude that the lateral sensitivity or footprint of the individual measurement series exceeds the coil dimension.

A full 2-D tomographic inversion of the four surface NMR measurements reproduces well the boundaries and water content of the perched water lens (Fig. 9). None of the inversion artifacts seen in the 1-D models are evident in the 2-D model. The lens boundary is correctly shown to be relatively sharp and water content within the lens body and surroundings is accurately reconstructed. The 2-D model is practically symmetric, verifying that the tomographic inversion scheme has properly accounted for the asymmetry of the data caused by the inclination of the Earth's magnetic field. The gradual transitions at the two ends of the reconstructed lens in Fig. 9 are a direct result of the applied smoothing.

4. Relaxation

In addition to supplying estimates of sub-surface water content surface NMR relaxation properties have the potential to provide other useful groundwater-related information. From borehole investigations of hydrocarbon reservoir rocks, empirical relations have been derived that relate NMR porosity and relaxation constants to hydraulic conductivity [33,34], a crucial parameter in hydro-geological studies. Although the range and type of data available from surface NMR techniques are more limited than those provided by borehole methods, the possibility of estimating hydraulic conductivities from surface NMR data is worth exploring.

4.1. Relaxation processes in rocks

In a bulk fluid a precessing proton transfers energy to its surrounding. This causes the proton to relax with the time constant T_1 into its low-energy state in which the proton precesses around an axis parallel to \mathbf{B}_0 . The relaxation of the transverse magnetization, with the time constant T_2 , is additionally affected by diffusion. Thus, T_2 is in general smaller than T_1 , but since diffusion is of minor importance

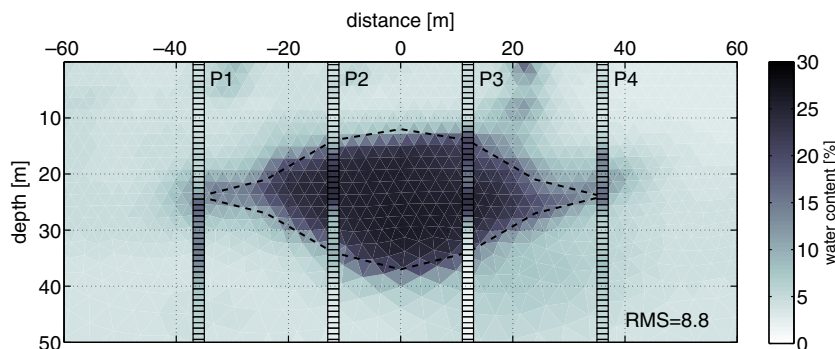


Fig. 9. Two-dimensional inversion result of the four coincident loop SNMR data sets simulated for the perched water lens model (see Fig. 6). The synthetic data are contaminated with 10 nV Gaussian noise (5%), comparable to that encountered under favorable field measurement conditions. The black dashed lines delineate the original model in Fig. 6, whereas the four discrete columns are the 1-D smooth inversions.

in homogeneous magnetic fields, T_2 approximately equals T_1 [33–36].

If water is captured in a porous rock, additional relaxation processes take place at the pore wall and both T_1 and T_2 are dramatically decreased. Protons close to the grain surface encounter fast magnetic relaxation with high probability. The cause of this relaxation is the presence of strong, highly localized magnetic fields, generated by unpaired electrons in paramagnetic atoms such as manganese and iron, which are attached to the negatively charged grain surface in many natural settings. As water molecules constantly diffuse through the pore space driven by Brownian motion, unrelaxed spins are delivered to the surface, while relaxed spins are moved from the surface into the open pore space. If the self-diffusion process is fast compared to the surface-induced relaxation, the overall relaxation will be averaged to a uniform mono-exponential decay throughout the pore [37].

Naturally, the relaxation strongly depends on the pore surface relaxivity, i.e. type and concentration of paramagnetic ions, but also on the pore size. In general, small pores are characterized by higher relaxation rates, i.e. shorter relaxation times, than large ones. A rock hosting a distribution of isolated pores of different size will exhibit a multi-exponential decay, due to the superposition of NMR signals in the record. In well coupled pore systems, however, as present in unconsolidated sediments, diffusion will transport molecules across several pores in relevant time-scales, leading to effectively averaged relaxation constants and thus to mono-exponential decay [38].

In practice, water molecules throughout the investigated volume may also be affected by slightly different macroscopic and microscopic magnetic fields independent of pore geometry, leading to slightly different Larmor frequencies (i.e. inhomogeneous spectral broadening in nuclear magnetic spectroscopy). The differing Larmor frequencies cause a substantial loss of phase coherence in the spin ensemble, and in consequence lead to a decreased transverse decay parameter T_2 . These biased values of the transverse relaxation time decay parameter are referred to as T_2^* .

4.2. Acquisition of relaxation parameters

NMR receiver coils pick up the superimposed magnetic effects of all transverse decay and dephasing mechanisms: the so-called free induction decay (FID). For this reason T_2^* is the decay parameter most easily extracted from NMR observations (Fig. 10a). Magnetic field gradients causing such dephasing occur at different scales, ranging from those from large geological or anthropogenic objects with high susceptibility, through gradients from features at the granular scale (e.g. from weathered hard rock), to internal gradients at the micro-scale caused by magnetized coating of inner pore surfaces. Such magnetic gradients have no influence on hydraulic properties. Consequently, FID-determined T_2^* values are rarely good proxies for host rock pore space properties and it is recommendable

to restrict oneself to T_1 and/or T_2 data when aiming for those targets.

In laboratory and borehole investigations, T_1 and T_2 can be determined indirectly by invoking various appropriate sequences of pulses at the Larmor frequency, for example the inversion recovery method [36]. Unfortunately, only approximate estimates of T_1 can be determined for sub-surface water protons with currently available surface NMR equipment [39,40].

The determination of relaxation constants by surface NMR is restricted by physical limitations: pulse sequences for T_1 and T_2 determination, that are well established in laboratory and borehole applications, are realized with secondary fields \mathbf{B}_1 , inducing tip angles of 90° and 180° . In surface NMR \mathbf{B}_1 is highly inhomogeneous throughout the investigated volume, making it difficult to achieve uniform tip angles for a large ensemble of spins, and thus preventing the use of sophisticated pulse sequences. Only an approximate estimate of T_1 can be determined for sub-surface water protons by applying a pseudo saturation recovery sequence: the spin magnetization V_0 , generated by the initial electromagnetic pulse will gradually relax towards its equilibrium state (Figs. 1 and 10a). During the decay of the signal generated by the first pulse, a second pulse is applied (in-phase or with arbitrary phase delay). The spin magnetization is tilted again and a second FID-determined V'_0 is measured. Under ideal conditions, when the first pulse is on-resonant and tips the spin vectors uniformly by 90° , the application of a second 90° -pulse leads to the same results as a common saturation recovery sequence (for the latter, see [34]). The transverse magnetization is not being saturated at all during this sequence. The longitudinal component, however, having recovered according to T_1 between two pulses, will be mapped into the (detectable) transverse plane by the second pulse, whereas the decayed transversal component will be mapped into the (non-detectable) longitudinal direction. The signal amplitude after the second pulse will carry information on T_1 , in dependence of the delay time between the pulses τ_d , obeying to $V'_0 = (1 - \exp(-\tau_d/T_1))V_0$.

The T_1 recovery curve is then estimated from just three points: (i) for a hypothetical pulse delay of zero the spin transverse magnetization is assumed to be fully saturated, i.e. $V_0^0 = 0$, (ii) the initial amplitude V'_0 at the delay time τ_d , (iii) the amplitude V_0 that has been measured after a single pulse is assumed to be equal to the asymptotic value of the relaxation process $V_0^\infty = V_0$.

4.3. Observed data

Fig. 11a shows experimental data of V'_0 for a range of q values and three delay times of 380, 480 and 680 ms, respectively (black, blue and red lines). V_0^∞ is determined from the asymptotic values at a delay time of 3600 ms (green line). Fig. 11b shows the results of fitting exponential curves to the various suites of recorded data. The T_1 estimates shown by dashed lines are based on three

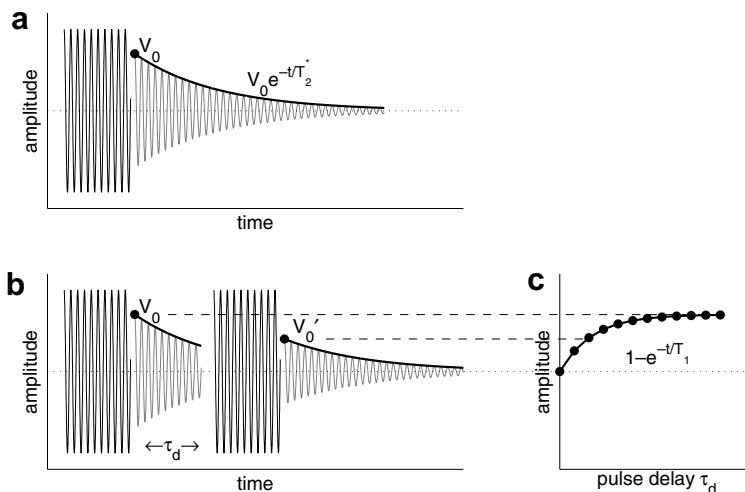


Fig. 10. Sketch of the NMR pseudo saturation recovery sequence. (a) From a single free induction decay (FID) experiment only the T_2^* relaxation time and initial amplitude V_0 can be determined. (b) Amplitudes V'_0 of individual free induction decay (FID) experiments are determined at increasing pulse delays to (c) achieve a recovery functional that increases as $(1 - \exp(-t/T_1))$. Modified from Ref. [51].

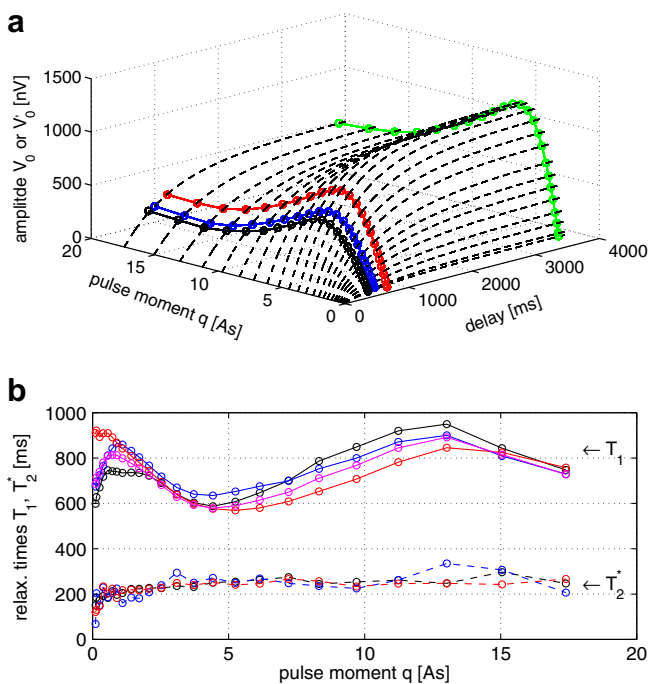


Fig. 11. (a) Surface NMR data recorded at the Haldensleben test site in Germany. For a range of pulse moments q : the green curve is the amplitude V_0 in Fig. 10 and the black, blue and red curves are amplitudes V'_0 in Fig. 10 for three different delay times $\tau_p = 380, 480$ and 680 ms. For each q value, the dashed line is the best-fit exponential function $(1 - \exp(t/T_1))$ to the four measured amplitudes (i.e. the points defining the black, blue, red and green curves) and the assumed zero amplitude at zero delay time. (b) For the same data set, the lower black, blue and red dashed lines are independent T_2^* estimates obtained for a range of pulse moments q . From the upper, the solid purple line represents the best-fit T_1 values determined from the dashed lines in (a). The solid black, blue and red lines are as for the purple line, but instead of using three different delay times in the construction of the exponential functions, only amplitudes for a single delay time are employed.

independent suites of V_0 values. The solid lines are T_1 estimates based on single second pulse measurements, at only

one τ_d each (black, blue and red lines), and estimates based on all three pulse delays (magenta line). The T_2^* values are roughly constant at ~ 300 ms for all pulse moments, whereas T_1 values vary between 600 and 900 ms over the range of pulse moments, indicating variations in sub-surface pore properties.

Several hydro-geological assessments have shown a good correlation of surface NMR T_1 -based hydraulic conductivities with those determined by pumping tests [40,41].

4.4. Limitations of current schemes

Currently, only one single second pulse at a single specific delay time is employed in surface NMR. This scheme only provides useful estimates of T_1 for mono-exponential signals and a high signal-to-noise ratio. To better constrain the exponential T_1 recovery curve for a multi-exponential analysis or limited data quality a series of V'_0 values must be recorded by repetition of the scheme for several delay times (Fig. 10).

For imperfect pulses (tilt angles others than 90°), the transverse magnetization after the second pulse is a more complex combination of T_1 and T_2 . However, since the major constituent of the recorded signal is induced by spins excited at or close to 90° , a first order approximation of the true T_1 can be made based on the acquired relaxation constants. Nevertheless, to derive robust estimates of pore properties from the surface NMR relaxation parameters, more reliable T_1 determination schemes are required and a better understanding of the effects of sub-surface inhomogeneities and resulting non- 90° tipping angles is needed. Furthermore, the basic assumption that T_1 can be calculated using a simplified saturation recovery formula is likely to be insufficient for separate transmitter and receiver loops. Fortunately, ongoing projects, involving more sophisticated modeling and inversion schemes, are

expected to yield improved determinations of T_1 in the near-future.

5. Limitations of the surface NMR method

5.1. Influence of the Earth's magnetic field

Significant variations in the magnitude and inclination of the Earth's magnetic field substantially influence the application of surface NMR methods worldwide. Prior to conducting a survey at any location, Larmor frequencies and induced magnetization levels can be estimated from the following relationships

$$\omega_L = -\gamma_p |\mathbf{B}_0|, \quad (51)$$

$$M = |\mathbf{B}_0| \frac{\gamma^2 \hbar^2 \rho_0}{4kT}, \quad (52)$$

both of which are linear functions of $|\mathbf{B}_0|$. Eq. (52) is known as Curie's Law for the spin magnetization, with γ the gyromagnetic ratio, \hbar Planck's constant, ρ_0 the spin density, k Boltzman's constant and T the absolute temperature in degrees Kelvin. According to Eqs. (23), (51) and (52), the surface NMR signal scales with the square of the Earth's magnetic field strength $|\mathbf{B}_0|^2$. The inclination enters the integral equation in a more complex way. It determines the perpendicular projection of the secondary field on the Earth's magnetic field direction, as it affects both the tip angle in the sine term of Eq. (23) and the sensitivity of the receiving field.

A map of estimated mean surface NMR signal response based on the global magnetic parameters (Fig. 12a and b) is shown in Fig. 12c. The values shown in this map are for a standard coincident loop measurement and are relative to a value in central Europe ($\mathbf{B}_0 = 48,000$ nT, inclination=65°). Fig. 12c demonstrates that amplitudes in south America can be as small as 25% of that in central Europe, whereas those typical in high northern and southern latitudes can be 150% of the mid-European value.

Fig. 13a–d show the dependency of the data kernel for a 45,000 nT Earth's magnetic field amplitude with inclination angles ranging from 0° (equator) to 90° (poles). The distribution of sensitivities throughout the range of pulse moments changes significantly. For low inclinations, the sensitivities are high at very low q values, but they decay rapidly as q increases. By contrast, for high inclination sites (polar regions) the sensitivities are more uniform throughout the range of q values.

Simulated sounding curves for a 100% water content throughout the sub-surface for magnetic inclinations 0°–90° are displayed in Fig. 13e–h. Each figure shows graphs for the Earth magnetic field strength ranging from 25,000 to 65,000 nT. Two important features can be observed from the series of amplitude versus q curves:

- The amplitude of the signal versus q curves in each figure scales with increasing Earth's field in a quadratic fashion as predicted from Eqs. (49) and (50).

- The pattern of the curves changes with inclination. The shape of the curves is a result of the pattern of the data kernels from Fig. 13a–d. At low inclinations the high sensitivities at low values of q cause a prominent peak at corresponding low q . With increasing inclination the more uniform data kernels lead to more uniform modeled amplitude versus q curves with a less pronounced peak at low values of q .

From Fig. 13a–d it is clear that local values of the Earth's magnetic field are important for expected surface NMR signals at any site worldwide. Employing the mean value of the amplitudes for a standard series of pulse moments allows one to determine the possibility of obtaining usable surface NMR data.

5.2. Influence of the sub-surface conductivity distribution

Electromagnetic fields generated by surface loops are, in general, affected by induction due to the conductivity of the ground. In earlier publications this resistivity influence has been related to the skin depth δ at the local Larmor frequency [16,42]. However, the skin depth is not appropriate for describing the induction effects in the near-field of surface NMR transmitter loops, since it is defined for plane waves incident at the Earth's surface [23], whereas propagation of the transmitted electromagnetic field in the vicinity of a loop is dominated by geometric spreading. Comprehensive modeling shows that the resistivity influence decreases with decreasing loop size, but for common combinations of loop size in the range of 5–150 m and ground resistivities between some few and several hundred Ωm , the resistivity influence is considerable and needs to be taken into account [43,44].

Real and imaginary parts of the data kernels for homogeneous ground resistivities in the 1000–1 Ωm range are displayed in Fig. 14a–h for a 100 m-diameter loop. At high resistivity of 1000 Ωm and 100 Ωm (Fig. 14a, b, e and f), there is no significant difference, either in the real or in the imaginary part. At a sub-surface resistivity of 10 Ωm (Fig. 14c and g) the real part of the data kernel is significantly attenuated in amplitude and depth penetration, while the imaginary part becomes quite large. For resistivity as low as 1 Ωm (Fig. 14d and h) these effects become even more pronounced. Data kernels are attenuated down to about 20% in depth penetration compared to their value at 1000 Ωm ; real and imaginary parts have comparable amplitudes.

The corresponding simulated measurement curves for a water content of 100% are shown in amplitude and phase form in Fig. 14i–p (solid lines and circles). The simulated measurements for purely insulative ground are shown (dashed lines) for comparison. With decreasing resistivity, progressively lower amplitudes and higher phase angles are observed. At very low resistivities of 1 Ωm the signal amplitudes for pulse moments larger than 5 As are attenuated down to unmeasurably small values. The resistivity

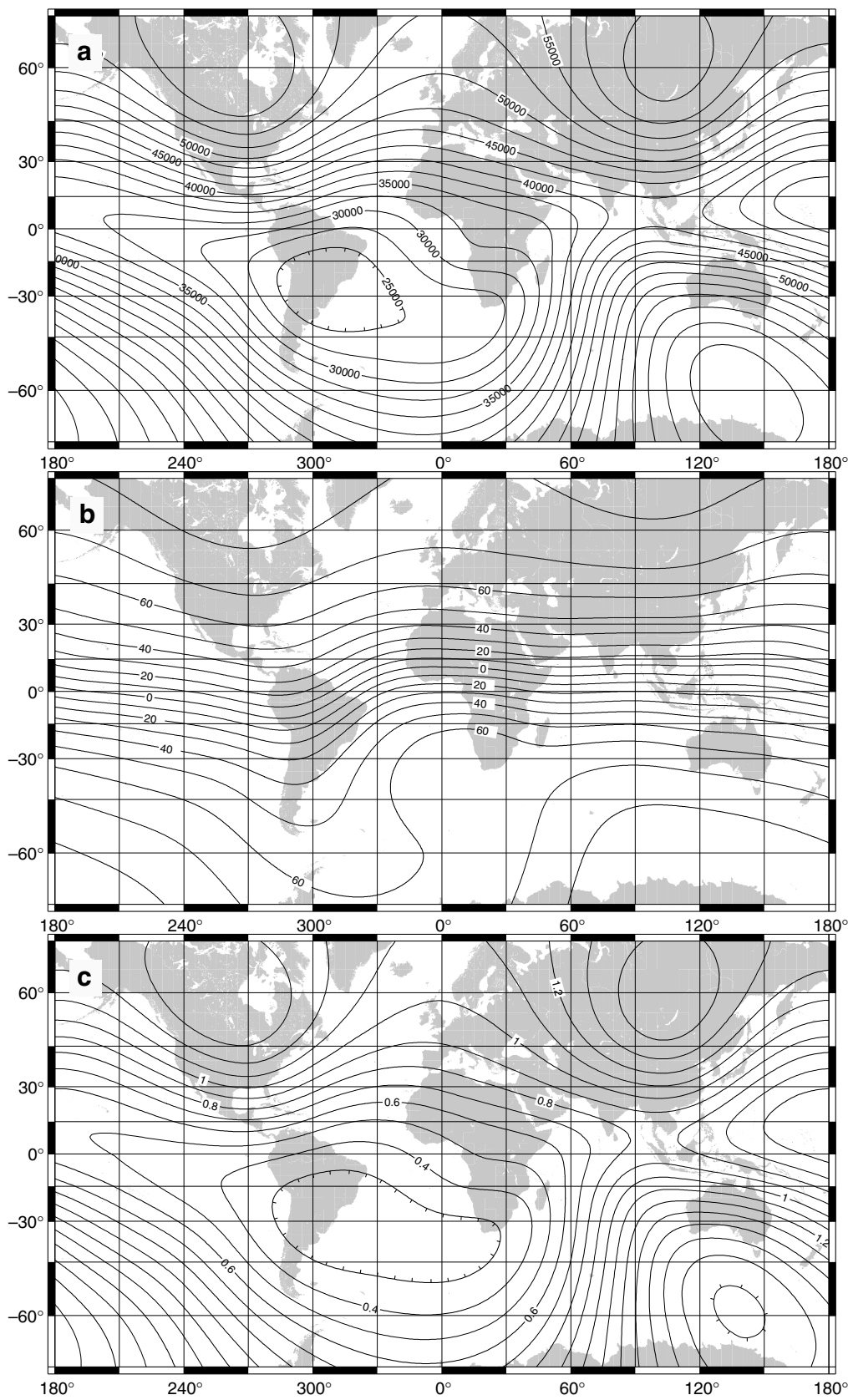


Fig. 12. Global maps showing the worldwide distribution of (a) the intensity B_0 and (b) the inclination I of the Earth's magnetic field. (c) The estimated worldwide surface NMR signal for coincident loop measurements normalized to mid-European conditions ($B_0 = 45,000$ nT, $I = 60^\circ$). (Maps compiled from WMM-2005 magnetic data, US-National Oceanic and Atmospheric Administration (NOAA), <http://www.ngdc.noaa.gov/seg/geomag>).

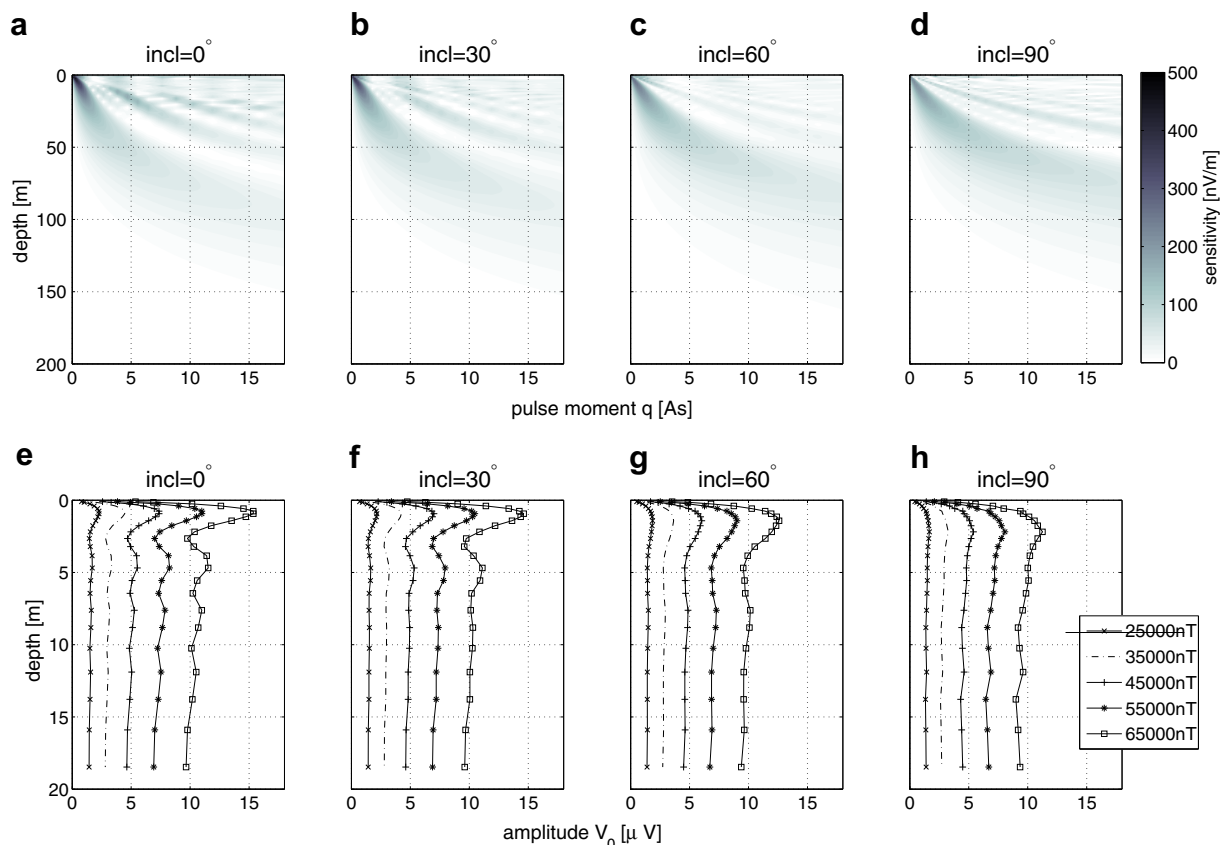


Fig. 13. (a–d) Surface NMR data kernels for an Earth's magnetic field intensity $B_0 = 45,000$ nT and inclinations $I = 0^\circ, 30^\circ, 60^\circ$ and 90° . (e–h) Synthetic measurements for 100% water content at inclinations $I = 0^\circ, 30^\circ, 60^\circ$ and 90° and the Earth's magnetic field intensity varying from 25,000 nT to 65,000 nT.

influence on surface NMR measurements becomes even more complex for inhomogeneous resistivity distributions in the sub-surface, either for 1-D resistivity stratification [45] or for 2-D or 3-D anomalous resistivity structures [46]. Thus, a priori knowledge of the sub-surface resistivity distribution is essential for the correct computation of the data kernel. Incorrect assumptions on the resistivity distribution can significantly affect the water content model that is derived by inversion with an incorrect kernel [47].

The imaginary part of the surface NMR signal exhibits interesting and complementary characteristics to the real part. For example it normally increases with decreasing resistivity, and generally has its maximum sensitivity at greater depth than does the real part. Therefore, by inverting complex surface NMR data involving complex kernels, there exists the potential for providing more complete information about the sub-surface [17].

6. Field data example

1-D surface NMR depth soundings have been acquired at a test site approximately 70 km east of Berlin in Germany. Here, the near-surface geology is represented by Quaternary glacial sediments consisting of alluvial sands, marls and glacial tills. At this test site the sedimentary stratification is well known from a nearby borehole and complementary near-surface geophysical measurements

[48]. A surface NMR measurement has been realized with a circular coincident loop for both transmitter and receiver with a diameter of 100 m, 1 turn, and a suite of 24 logarithmically spaced pulse moments ranging from 0.25 to 18.5 As. The recorded data displayed in Fig. 15 show signal amplitudes in the range of 600–1200 nV with a maximum at a pulse moment of about 1 As. The corresponding T_2^* relaxation constants range from below 200 ms for small pulse moments and increase up to 300 ms for larger pulse moments. The signal phase shows a pattern that cannot be explained by induction effects of the loop magnetic fields. The obvious correlation with the signal-derived Larmor frequency indicates that the major effect of the phase is caused by off-resonant excitation of the proton spins and off-resonant recording in the resonance-tuned receiver loop. These technically induced phase shifts in the recorded signal make the complex signal basically unusable for inversion. The amplitude, however, is not affected by these off-resonance effects and the subsequent assessment of inversion schemes on this data set is based on amplitude data alone.

Applying the fixed-boundary inversion scheme to the data set in Fig. 15 and using the bootstrapping procedure for assessment of the reliability of the model gives the suite of inversions in Fig. 16a. The models indicate a shallow aquifer from 2 m down to approximately 15 m with a water content of around 25% above a layer of low water content

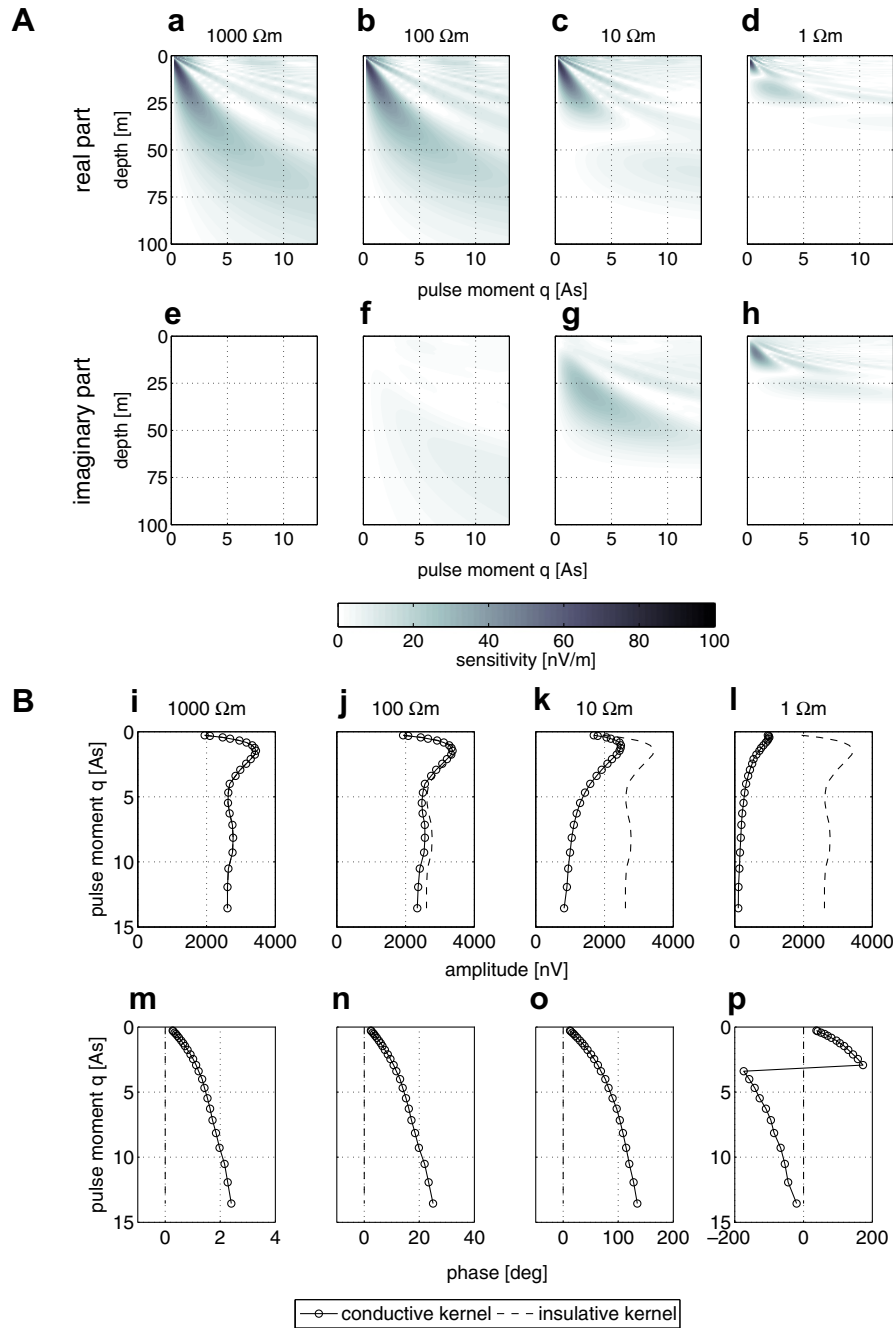


Fig. 14. (A) Surface NMR data kernels showing real and imaginary parts for ground of homogeneous sub-surface resistivities ranging from 1000–1 Ωm. (B) Synthetic measurements 100% water content within ground with homogeneous sub-surface resistivities ranging from 1000–1 Ωm (black lines and circles) and corresponding measurements for perfectly resistive ground (dashed lines).

from 15 to 30 m. At 30 m the water content rises to a second series of two aquifers with maximum water contents of 18% and 22% at depth of 35 m and 62 m, respectively. These aquifers are interbedded with a layer of slightly lower water content at a depth of 45 m. Bootstrapping of the data, based on studentized residuals as introduced in Section 3.1.3, gives only slight variations in the series of inverted water content models.

Using the inversion scheme of variable-boundary inversion for the same data set with a model geometry derived from the fixed-boundary inversion to have six layers yields

the inversion results in Fig. 16b. The models show a similar sub-surface water content distribution, with three units of high water content, enclosed within confining beds of low water content. The six layer model exhibits some differences to the fixed-boundary model: (i) whereas the fixed-boundary model shows a thin layer of low water content close to the Earth's surface, the variable-boundary model cannot resolve this, (ii) the aquifer at 30–40 m depth in the variable-boundary model shows significantly higher water content than the equivalent one in the model of fixed geometry, (iii) water contents of the confining beds are gen-

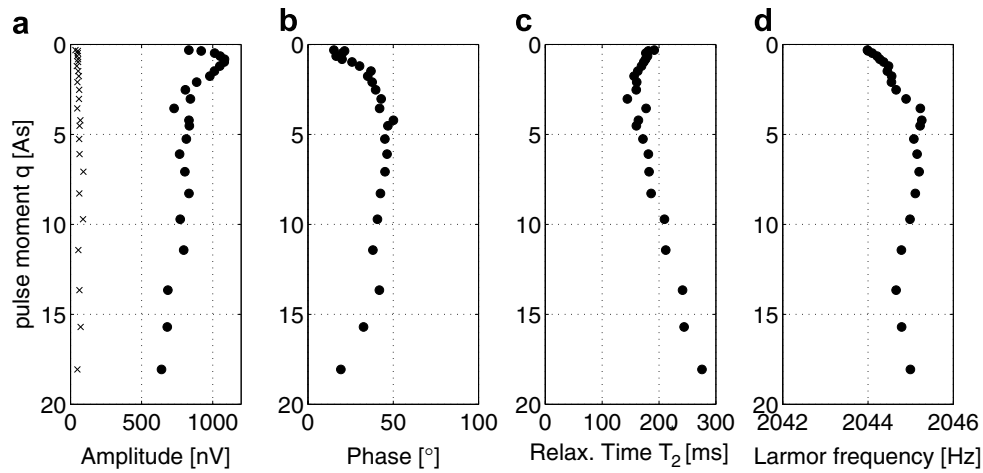


Fig. 15. Recorded surface NMR data at the test site east of Berlin. The complex signal amplitude versus pulse moment is plotted in amplitude (a) and phase (b). Additionally the derived relaxation time constant T_2 (c) and the variation of the Larmor frequency (d) during the measurement due to diurnal variations of the Earth’s magnetic field is shown.

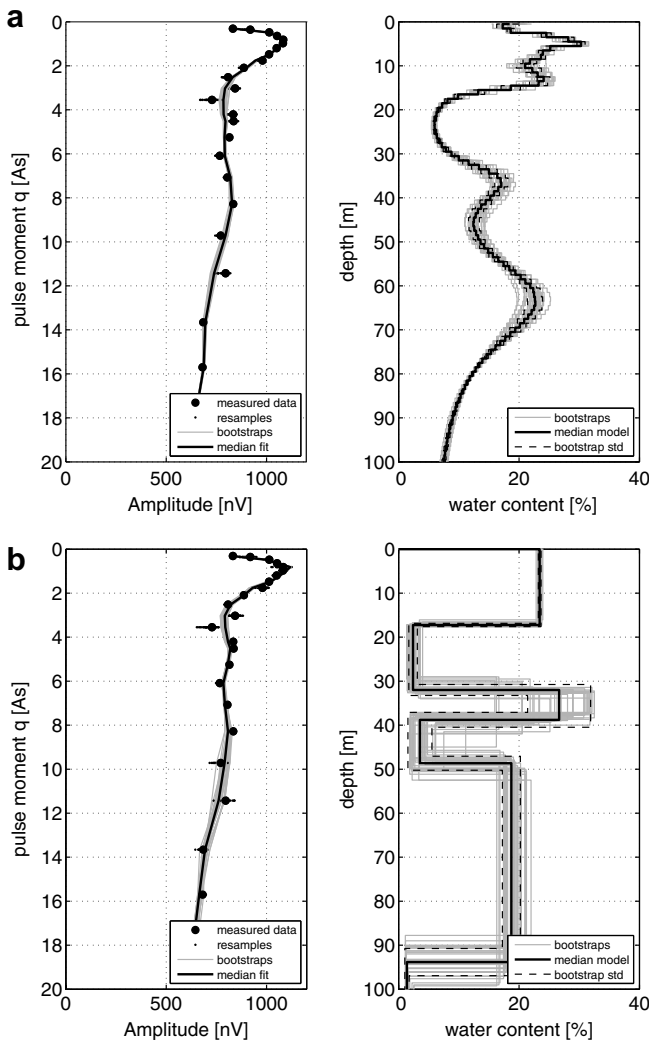


Fig. 16. Bootstrap analysis of the data set in Fig. 15 for (a) the fixed layer inversion scheme and (b) the variable layer inversion scheme.

erally lower in the variable geometry model than in the fixed-boundary one.

The bootstrapped results of the variable-boundary model show a higher variability and consequently a higher standard deviation than the fixed-boundary model. However, the series of bootstrapped inversion yields consistent results indicating that the data are fitted best by the assumed model geometry with six layers.

Results of both inversion schemes are compared in Fig. 17. The following observations can be made: (i) the synthetic measurements based on the two median models of variable and fixed-boundary inversion fit the measured data equally well, (ii) the main structures of the derived models basically coincide within their systematic limitations and show the segmentation into three individual aquifers, interbedded with confining beds. The fixed-boundary inversion, however, heavily smoothes thin layers in particular and makes a quantitative interpretation of aquifer properties concerning boundaries and water contents impossible. The variable-boundary inversion shows a much sharper distinction of aquifer boundaries and allows quantitative estimates of aquifer water contents.

Comparison of the inversion results with the aquifer structure (dark gray patch plots in Fig. 17b) that are derived from the borehole logs at the right-hand side, gives a fairly good correlation. Both inversion results delineate the complex aquifer structure to a satisfactory degree. The estimated water contents are in good agreement with expected aquifer properties in these Quarternary glacial deposits. The borehole extends down to a depth of 60 m. At about 54 m after a loss of core material for some 2 m, Tertiary sediments have been found that consist of well-sorted marine sands. Hence, no significant change of aquifer properties is found at this geological boundary, but the Tertiary sediments are assumed to continue as a quite homogeneous layer. The lower boundary of the third aquifer interpreted from surface NMR inversion at a depth of 81 m is below the extent of the borehole and thus cannot be confirmed. Additionally, the sensitivity of the surface NMR method does not allow a reliable prediction of the

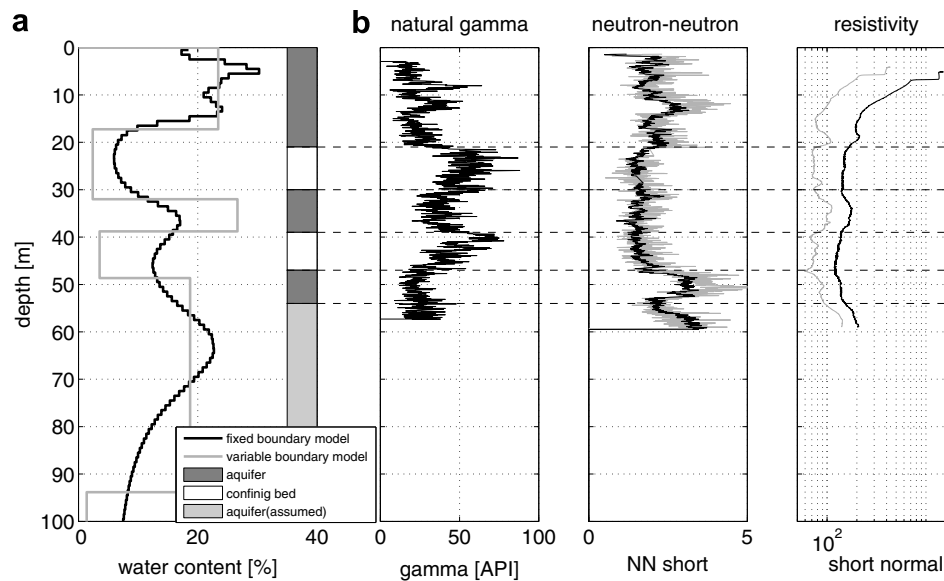


Fig. 17. (a) Median models of water content distribution with depth from Fig. 16, obtained by fixed and variable-boundary inversion schemes compared to interpreted aquifer stratification from borehole data. (b) Borehole logs of the research drill-hole in about 150 m distance from the measurement loop center.

boundaries and/or water contents at this depth. Even though a fairly good reproduction of this boundary with both inversion schemes is given, the existence and reliability of this layer boundary should be treated with care.

Note that throughout the resistivity log the regions of high water content are characterized by increased values of resistivity, but variations are too small to be resolved by means of surface geoelectrical or electromagnetic methods [49].

7. Summary and conclusions

This review has provided information about the various aspects of surface NMR. In the first section the most basic formulation is presented which reveals the complexity of the forward functional. For the quantitative description of the surface NMR signal the interaction of the spin system with the non-uniform, non-perpendicular and elliptically polarized secondary field is taken into account. Furthermore, for configurations with non-coincident transmitter and receiver loops, the vectorial relation of the spin magnetization to these fields was considered. This allows a complete forward functional with suitable formulations for 1-D and 2-D conditions to be derived by integrating the data kernel of the forward functional to the respective dimensions. In the second section these data kernels are the basis for the inversion of surface NMR measurements to reconstruct models of sub-surface water content distribution. Besides a least-squares inversion of a model with a large number of layers and variable but constrained water content, which is most common in geophysical data inversion, a novel scheme with a small number of discrete layers whose boundaries are allowed to vary in depth is presented. Both schemes provide comparable

models. Comparing these two approaches, the variable-boundary model gives a better quantification of the depths of layer boundaries and estimates of layer water content than does the model with fixed boundaries. But inversion with such a scheme can only provide useful sub-surface information if the variation of the water content in the sub-surface is sharp rather than gradational, and if an estimate of the number of geological units is known beforehand. Inversion of field data is in general ambiguous. This is particularly so in cases where there are considerable uncertainties in the measured data, which often occurs for the weak surface NMR signals in the presence of strong ambient background noise. A bootstrapping scheme applied to surface NMR inversion is introduced in Section 3. It provides a suitable tool to assess the ambiguity of the model of water content distribution and allows the assignment of confidence intervals for the shown example. In many NMR applications the relaxation time is the major source of information on properties of the object under investigation. Also in NMR applied to geo-materials the relaxation time can be a useful measure to estimate structural parameters, but determination of the sub-surface distribution of the relaxation constants is physically limited and technically challenging for surface NMR. In Section 4 the available techniques used for surface NMR are explained. It is demonstrated that in sedimentary environments the most easily accessible relaxation time T_2^* is rarely a valuable measure for host rock properties. In any case quantitative formulations for the derivation of T_1 relaxation from surface NMR measurements are not yet available. The two inversion schemes and the bootstrapping techniques are applied to a real data example in Section 6. From both inversion schemes a consistent model of 1-D aquifer stratification is obtained. The comparison to

borehole data from a nearby research drill-hole shows the capability and almost unique potential of the surface NMR technique in resolving discrete water-bearing zones. A model of similar spatial resolution of the water content distribution can only be interpreted by the combination of a series of borehole measurements, but can definitely not be obtained by any other surface geophysical technique.

The development of surface NMR has undergone a rapid progress over the last two decades. Nowadays it has reached a mature phase in terms of available hardware, theoretical description of the forward functional and advanced inversion techniques. However, major topics for further research lie in (i) forward calculation of the loop magnetic fields in more complex environments such as varied topography or spatially complex resistivity distribution within the sub-surface; (ii) the quantitatively more precise formulation of the spin dynamics in the weak magnetic field of the Earth and the non-uniform loop fields and (iii) establishing reliable correlations of surface NMR determined relaxation times and hydro-geological parameters. A major drawback of applying surface NMR to groundwater studies is the presence of background noise. Typical signal amplitudes of surface NMR measurements are very weak and cannot be easily increased relative to the ambient noise level by technical means. Hence, surface NMR measurements are nowadays not feasible in many environments. Ongoing research by several groups worldwide, aimed at understanding, describing and recording surface NMR signals offers promise of further improvement. However, restriction to low noise environments will probably be the major issue and pose the greatest challenge to widespread acceptance of this promising technique in the near-future.

Acknowledgements

This research has benefitted greatly from constructive discussions I had with my colleagues in both ETH Zurich and Technical University of Berlin. There are far too many individuals to personally acknowledge but I especially thank Prof. A. Green for his support and incisive review of the manuscript.

References

- [1] R. Varian, Ground liquid prospecting method and apparatus, US Patent 3019383, 1962.
- [2] A. Semenov, NMR hydroscope for water prospecting, in: Proceedings of the Seminar on Geotomography, 1987, pp. 66–67.
- [3] A. Semenov, A. Burshtein, A. Pusep, M. Schirov, A device for measurements of underground mineral parameters, USSR Patent 1079063, 1988 (in Russian).
- [4] A. Semenov, M. Schirov, A. Legchenko, A. Burshtein, A. Pusep, Device for measuring the parameter of underground mineral deposits, Great Britain, Patent 2198540B, 1989.
- [5] M. Schirov, A. Legchenko, G. Creer, A new direct non-invasive groundwater detection technology for Australia, Exploration Geophysics 22 (1991) 333–338.
- [6] M. Goldman, B. Rabinovich, M. Rabinovich, D. Gilad, I. Gev, M. Schirov, Application of the integrated NMR-TDEM method in groundwater exploration in Israel, Journal of Applied Geophysics 31 (1994) 27–52.
- [7] I. Gev, M. Goldman, B. Rabinovich, M. Rabinovich, A. Issar, Detection of the water level in fractured phreatic aquifers using nuclear magnetic resonance (NMR) geophysical measurements, Journal of Applied Geophysics 33 (1996) 277–282.
- [8] O. Shushakov, Groundwater NMR in conductive water, Geophysics 61 (4) (1996) 998–1006.
- [9] A. Legchenko, P. Valla, Processing of surface proton magnetic resonance signals using non-linear fitting, Journal of Applied Geophysics 39 (1998) 77–83.
- [10] A. Legchenko, O. Shushakov, Inversion of surface NMR data, Geophysics 63 (1) (1998) 75–84.
- [11] P. Valla, A. Legchenko, Surface nuclear magnetic resonance – what is possible, Journal of Applied Geophysics 50 (2002) 1–229.
- [12] U. Yaramanci, A. Legchenko, Magnetic resonance sounding, aquifer detection and characterization, Near Surface Geophysics 3 (2005) 119–222, 255–310.
- [13] T. Radic, Zeitreihenwertung von nmr messungen im erdmagnetfeld, in: O. Ritter, H. Brasse (Ed.), 21. EMTF-Kolloquium 2005 in Holle, Germany, 2005.
- [14] D.O. Walsh, Multi-dimensional surface nmr imaging and characterization of selected aquifers in the western US, in: Eos Trans. AGU, vol. 87, Fall Meet. Suppl., Abstract NS41A-1134, 2007.
- [15] P.B. Weichman, E.M. Lavelly, M. Ritzwoller, Surface nuclear magnetic resonance imaging of large systems, Physical Review Letters 82 (20) (1999) 4102–4105.
- [16] P.B. Weichman, E.M. Lavelly, M.H. Ritzwoller, Theory of surface nuclear magnetic resonance with applications to geophysical imaging problems, Physical Review E 62 (1, Part B) (2000) 1290–1312.
- [17] M. Braun, M. Hertrich, U. Yaramanci, Complex inversion of MRS data, Near Surface Geophysics 3 (3) (2005) 155–163.
- [18] M. Hertrich, Magnetic resonance sounding with separated transmitter and receiver loops for the investigation of 2d water content distributions, Ph.D. thesis, School of Civil Engineering and Applied Geosciences, Technical University of Berlin, 2005.
- [19] M. Hertrich, M. Braun, U. Yaramanci, Magnetic resonance soundings with separated transmitter and receiver loops, Near Surface Geophysics 3 (3) (2005) 131–144.
- [20] M. Hertrich, M. Braun, T. Günther, A.G. Green, U. Yaramanci, Surface nuclear magnetic resonance tomography, Geoscience and Remote Sensing, IEEE Transactions on 45 (11) (2007) 3752–3759.
- [21] J. Jackson, Klassische Elektrodynamik, de Gruyter, Berlin, 1983.
- [22] A. Abragam, Principles of nuclear magnetism, Oxford University Press, 1983.
- [23] S.H. Ward, G.W. Hohmann, Electromagnetic theory for geophysical applications, in: M.N. Nabighian (Ed.), Electromagnetic Methods in Applied Geophysics, Investigations in Geophysics, vol. 1, Soc. Expl. Geophys., 1988, Chapter 4, pp. 131–311.
- [24] R.C. Aster, B. Borchers, C.H. Thurber, Parameter Estimation and Inverse Problems, Elsevier Academic Press, 2005.
- [25] A. Guillen, A. Legchenko, Application of linear programming techniques to the inversion of proton magnetic resonance measurements for water prospecting from the surface, Journal of Applied Geophysics 50 (1–2) (2002) 149–162, special issue.
- [26] A. Guillen, A. Legchenko, Inversion of surface nuclear magnetic resonance data by an adapted Monte Carlo method applied to water resource characterization, Journal of Applied Geophysics 50 (1–2) (2002) 193–205.
- [27] O. Mohnke, U. Yaramanci, Smooth and block inversion of surface NMR amplitudes and decay times using simulated annealing, Journal of Applied Geophysics 50 (1–2) (2002) 163–177.
- [28] P.B. Weichman, D.R. Lun, M.H. Ritzwoller, E.M. Lavelly, Study of surface nuclear magnetic resonance inverse problems, Journal of Applied Geophysics 50 (1–2) (2002) 129–147.

- [29] M. Hertrich, U. Yaramanci, Joint inversion of surface nuclear magnetic resonance and vertical electrical sounding, *Journal of Applied Geophysics* 50 (1–2) (2002) 179–191.
- [30] T. Günther, C. Rücker, K. Spitzer, Three-dimensional modelling and inversion of dc resistivity data incorporating topography - II. Inversion, *Geophysical Journal International* 166 (2) (2006) 506–517.
- [31] W. Menke, *Geophysical Data Analysis: Discrete Inverse Theory*, Revised Edition, International Geophysics Series, vol. 45, Academic Press, San Diego, CA, 1989.
- [32] B. Efron, R. Tibshirani, *An Introduction to the Bootstrap*, Chapman & Hall, New York, 1993.
- [33] W.E. Kenyon, Petrophysical principles of applications of nmr logging, *The Log Analyst* (1997) 21–43.
- [34] K.-J. Dunn, D.J. Bergman, G.A. Latorraca, *Nuclear Magnetic Resonance*, first ed., Pergamon, 2002.
- [35] G. Coates, L. Xiao, M. Prammer, *NMR Logging Principles and Application*, Halliburton Energy Services, 1999.
- [36] M.H. Levitt, *Spin Dynamics – Basics of Nuclear Magnetic Resonance*, John Wiley & Sons, Ltd, 2002.
- [37] K.R. Brownstein, C.E. Tarr, Importance of classical diffusion in nmr studies of water in biological cells, *Physical Review A* 19 (1979) 2446–2453.
- [38] K.R. McCall, D.L. Johnson, R. Guyer, Magnetization evolution in connected pore systems, *Physical Review B* 44 (14) (1991) 7344–7355.
- [39] A. Legchenko, J.-M. Baltassat, A. Beauce, J. Bernard, Nuclear magnetic resonance as a geophysical tool for hydrogeologists, *Journal of Applied Geophysics* 50 (1–2) (2002) 21–46.
- [40] A. Legchenko, J.-M. Baltassat, A. Bobachev, C. Martin, H. Robain, J.-M. Vouillamoz, Magnetic resonance sounding applied to aquifer characterization, *Ground Water* 42 (3) (2004) 363–373.
- [41] J.-M. Vouillamoz, M. Descloitres, G. Toe, A. Legchenko, Characterization of crystalline basement aquifers with MRS: comparison with boreholes and pumping tests data in Burkina Faso, *Near Surface Geophysics* 3 (3) (2005) 205–213.
- [42] J. Vouillamoz, B. Chatenoux, F. Mathieu, J. Baltassat, A. Legchenko, Efficiency of joint use of MRS and VES to characterize coastal aquifer in Myanmar, *Journal of Applied Geophysics* 61 (2) (2007) 142–154.
- [43] M. Hertrich, M. Mueller-Petke, U. Yaramanci, Potential of the application of magnetic resonance sounding to deep targets, in: *Proceedings of the 3rd International Workshop on MRS, Madrid/Spain, 2006*, pp. 41–44.
- [44] M. Braun, Influence of the resistivity on magnetic resonance sounding: 1d inversion and 2d modelling, Ph.D. thesis, Fakultät VI Planen Bauen Umwelt, Technical University of Berlin, 2007.
- [45] M. Braun, U. Yaramanci, Inversions of Surface-NMR signals using complex kernels, in: *Proceedings of the 9th EEGS Conference, Prague/Czech Republic, 2003*, pp. 0–49.
- [46] M. Braun, I. Rommel, U. Yaramanci, Modelling of magnetic resonance sounding using finite elements (femlab) for 2d resistivity extension, in: *Proceedings der Femlab Konferenz 2005*, No. ISBN 3-00-017211-4, 2005, pp. 191–196.
- [47] D. Trushkin, O. Shushakov, A. Legchenko, Surface NMR applied to an electroconductive medium, *Geophysical Prospecting* 43 (1995) 623–633.
- [48] U. Yaramanci, G. Lange, M. Hertrich, Aquifer characterisation using surface NMR jointly with other geophysical techniques at the Nauen/Berlin test site, *Journal of Applied Geophysics* 50 (1–2) (2002) 47–65.
- [49] J. Goldbeck, Hydrogeophysical methods at the test-site Nauen – evaluation and optimisation, Diplomarbeit, Technische Universität Berlin, 2002.
- [50] U. Yaramanci, M. Hertrich, Magnetic resonance sounding, in: R. Kirsch (Ed.), *Groundwater Geophysics*, Springer, 2006, pp. 253–273.
- [51] O. Mohnke, U. Yaramanci, Forward modeling and inversion of MRS relaxation signals using multi-exponential decomposition, *Near Surface Geophysics* 3 (3) (2005) 165–185.